BIOMACROMOLECULES

Direct Radiolabeling of Trastuzumab-Targeting Triblock Copolymer Vesicles with ^{89}Zr for Positron Emission Tomography Imaging

Veronika Kozlovskaya,[⊥] Maxwell Ducharme,[⊥] Maksim Dolmat, James M. Omweri, Volkan Tekin, Suzanne E. Lapi, and Eugenia Kharlampieva[*]

Cite This: Biomacromolecules 2023, 24, 1784−1797

Read Online

ACCESS | Metrics & More | Article Recommendations | Supporting Information

Downloaded via UNIV OF ALABAMA BIRMINGHAM on April 10, 2023 at 17:19:53 (UTC).
See https://pubs.acs.org/sharingguidelines for options on how to legitimately share published articles.

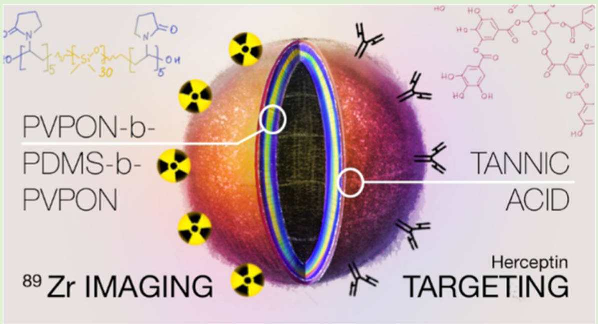

ABSTRACT: Radiolabeled drug nanocarriers that can be easily imaged *via* positron emission tomography (PET) are highly significant as their *in vivo* outcome can be quantitatively PET-traced with high sensitivity. However, typical radiolabeling of most PET-guided theranostic vehicles utilizes modification with chelator ligands, which presents various challenges. In addition, unlike passive tumor targeting, specific targeting of drug delivery vehicles *via* binding affinity to overexpressed cancer cell receptors is crucial to improve the theranostic delivery to tumors. Herein, we developed ^{89}Zr-labeled triblock copolymer polymersomes of 60 nm size through chelator-free radiolabeling. The polymersomes are assembled from poly(*N*-vinylpyrrolidone)$_5$-*b*-poly(dimethylsiloxane)$_{30}$-*b*-poly(*N*-vinylpyrrolidone)$_5$ (PVPON$_5$-PDMS$_{30}$-PVPON$_5$) triblock copolymers followed by adsorption of a degradable tannin, tannic acid (TA), on the polymersome surface through hydrogen bonding. TA serves as an anchoring layer for both ^{89}Zr radionuclide and targeting recombinant humanized monoclonal antibody, trastuzumab (Tmab). Unlike bare PVPON$_5$-PDMS$_{30}$-PVPON$_5$ polymersomes, TA- and Tmab-modified polymersomes demonstrated a high radiochemical yield of more than 95%. Excellent retention of ^{89}Zr by the vesicle membrane for up to 7 days was confirmed by PET *in vivo* imaging. Animal biodistribution using healthy BALB/c mice confirmed the clearance of ^{89}Zr-labeled polymersomes through the spleen and liver without their accumulation in bone, unlike the free nonbound ^{89}Zr radiotracer. The ^{89}Zr-radiolabeled polymersomes were found to specifically target BT474 HER2-positive breast cancer cells *via* the Tmab-TA complex on the vesicle surface. The noncovalent Tmab anchoring to the polymersome membrane can be highly advantageous for nanoparticle modification compared to currently developed covalent methods, as it allows easy and quick integration of a broad range of targeting proteins. Given the ability of these polymersomes to encapsulate and release anticancer therapeutics, they can be further expanded as precision-targeted therapeutic carriers for advancing human health through highly effective drug delivery strategies.

■ INTRODUCTION

Breast cancer is among the world's most common cancer diseases and represents 25% of other cancers.[1] Despite many advancements in breast cancer treatment, its global rates of mortality are still high.[2] Current breast cancer chemotherapies include the systemic delivery of free drugs or therapeutic antibodies and have been often associated with cardiotoxicity and cardiac dysfunction.[3] Imaging-guided drug delivery is a noninvasive alternative to direct injection of drugs into tumors and systemic free drug delivery and can allow an effective drug activity with reduced dose toxicity.[4−9] In this type of delivery, molecular imaging can be used to follow drugs with clinically relevant imaging protocols and precisely tailored to a specific spatial and temporal regimen. Among widely used imaging methods, including optical imaging[10] and magnetic resonance (MRI),[11] positron emission tomography (PET) is advantageous in performing noninvasive clinical imaging of a whole body and ensuring drug delivery to tumors.[12,13] PET has high sensitivity and quantitation due to the use of small amounts of radionuclides (radiotracers) and has been widely exploited for tracking the biodistribution of nanomaterials *in vivo*.[14]

PET radiolabeling of therapeutic molecules and nanomaterials usually includes coupling of chelating ligands including 1,4,7,10-tetraazacyclododecane-1,4,7,10-tetraaceticacid (DOTA) or desferrioxamine (DFO) that produce stable coordination bonds with radioisotope ions (*e.g.*, ^{68}Ga, ^{64}Cu, ^{89}Zr, ^{52}Mn)[15] beneficial for quantitative tracking of the *in vivo* behavior and metabolism of the therapeutics.[16−19] The short half-lives of ^{68}Ga (67.7 min half-life) and ^{64}Cu (12.7 h half-

Received: December 31, 2022
Revised: March 3, 2023
Published: March 16, 2023

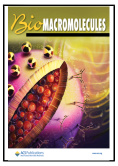

ACS Publications © 2023 American Chemical Society

https://doi.org/10.1021/acs.biomac.2c01539

life), however, might not be applicable for the development of PET image-guided therapeutic nanocarriers desirable for a long-term tracing of the nanocarrier *in vivo* outcomes.[20] The radioisotopes with much longer half-lives, including ^{89}Zr (3.3 days), ^{52}Mn (5.6 days), or ^{124}I (4.18 days), would be more suitable for imaging long-term nanoparticle circulation, specific targeting, and drug release. The signal intensity and resolution of PET images are also dependent on the positron ranges defining radionuclide tissue penetration. While high-energy positrons penetrate larger distances from the emission source before annihilation, they can produce images with reduced spatial resolution. Among ^{89}Zr, ^{52}Mn, and ^{124}I, with the corresponding average positron ranges in the tissues of 1.23, 0.63, and 3.48 mm, ^{89}Zr has a good balance between longer-term imaging and good spatial resolution.[21]

Polymeric nanocarriers have been shown to be advantageous as theranostic agents that can easily combine imaging (diagnostic) and therapeutic functions.[22,23] Unlike single-molecule therapeutics conjugates and rigid organic or inorganic nanoparticles, which can have low blood circulation, tissue toxicity, low drug loading, and adverse immune responses, soft polymeric vesicles (polymersomes) assembled from amphiphilic block copolymers demonstrated high therapeutic payloads and can be obtained as biocompatible and biodegradable with various functionalities providing environmental stimuli-induced responses.[24] In contrast to phospholipid vesicles (liposomes) that may suffer short circulation half-lives, low mechanical stability *in vivo*,[25] drug leakage, and fusion,[26] the block copolymers provide excellent control over the polymersome structure and physicochemical properties.[27−32] For example, varying the polymerization degree of the hydrophilic blocks in poly(*N*-vinylcaprolactam)$_n$-*b*-poly(dimethylsiloxane)$_m$-*b*-poly(*N*-vinycaprolactam)$_n$ (PVCL$_n$-PDMS$_m$-PVCL$_n$) and poly(*N*-vinylpyrrolidone)$_n$-*b*-PDMS$_m$-*b*-poly(*N*-vinylpyrrolidone)$_n$ (PVPON$_n$-PDMS$_m$-PVPON$_n$) triblock copolymers while keeping the ratio of PDMS/PVCL or PDMS/PVPON was shown to modulate the size of small (<500 nm) vesicles where increasing the length of the hydrophilic block decreased the size of a small vesicle.[33−35] A superior *in vivo* stability of synthetic polymersomes assembled from poly(3-methyl-*N*-vinylcaprolactam)-*b*-poly(*N*-vinylpyrrolidone) over liposomes has been shown to decrease doxorubicin-induced cardiotoxicity.[36]

In addition, the availability of various functional groups for the modification of polymer nanoparticles with active biological molecules (binding ligands) has been shown to be crucial for enhanced tumor targeting and uptake through specific binding of these ligands to overexpressed receptors on target cells.[37,38] Trastuzumab (Tmab), a humanized monoclonal antibody, is approved as a therapy against breast cancers with overexpressed human epidermal receptor 2 (HER2), which makes up about 30% of invasive breast cancer patients.[39] Tmab has been extensively studied as a targeting ligand for HER2 cancer cells.[40]

Chelator-based radiolabeling of synthetic polymer vesicles, however, may present various challenges hampering the development of image-guided drug nanocarriers, including multistep modification and purification with chelator molecules, limited choice of chelator ligands, transchelation, possible release of the chelator molecules, and free radiotracers *in vivo*, and adversely altering the surface properties of the drug vehicles resulting in biodistribution changes.[41−44] Conversely, chelator-free radiolabeling can provide direct integration of the radiotracers to delivery vehicles mitigating the above challenges. Previously, direct radiolabeling was demonstrated through doping of inorganic nanoparticles with radionuclides (^{64}Cu) during nanoparticle synthesis,[45] *via* mixing of a PET tracer (^{89}Zr) with metal oxides,[46] direct adsorption of arsenic isotopes to nanoparticle surfaces through specific interactions,[47] through binding oxophilic radiotracers to silica nanoparticles,[48] and binding of ^{68}Ga and ^{64}Cu to zinc sulfide quantum dots through cation exchange.[49] While these methods primarily concern inorganic nanoparticles, they might also result in the loss of radioactivity, changes in surface properties, and transchelation.[45,47,48]

Chelator-free radiolabeling of nanocapsule delivery vehicles, including liposomes,[50] exosomes,[51] and polymersomes,[44] has been demonstrated mainly through the radiotracer encasement within the interior cavity[44,51] or nanocapsule membrane, causing poor retention of the radionuclide in serum *in vivo*. Therefore, a reliable and simple approach for chelator-free labeling of polymeric nanovesicles with stable retention of a radiotracer is desirable for *in vivo* applications. We have shown previously that polymer nanovesicles can be obtained by self-assembly of the poly(*N*-vinylpyrrolidone)$_5$-*b*-poly(dimethylsiloxane)$_{30}$-*b*-poly(*N*-vinylpyrrolidone)$_5$ (PVPON$_5$-PDMS$_{30}$-PVPON$_5$) triblock copolymer through a solvent-exchange method (nanoprecipitation).[35] Polymeric nanovesicles from a similar triblock copolymer PVPON$_{14}$-PDMS$_{47}$-PVPON$_{14}$ were demonstrated to efficiently encapsulate and deliver PARP1 siRNA to successfully knock down PARP1 *in vivo*.[52] We have also demonstrated that hydrogen bonding interactions between the polyphenol, tannic acid (TA), and PVPON stable at physiological pH[53] have the potential as an antioxidant and immunomodulatory coating.[54−57]

Our previous work with poly(*N*-vinylcaprolactam)-*b*-PDMS-*b*-poly(*N*-vinylcaprolactam) (PVCL-PDMS-PVCL) triblock copolymer and PVCL-*b*-PVPON diblock copolymer polymersomes demonstrated biocompatibility and noncytotoxicity of these materials (*i.e.*, PDMS and PVPON) *in vitro*[33,58] and *in vivo*.[36,59] Moreover, no cytotoxicity was found when TA was complexed with PVPON in PVCL-PVPON diblock copolymer polymersomes[59] and in (TA/PVPON) multilayer microcapsules both *in vitro* and *in vivo*.[55−57]

In this study, we have developed a simple approach for a chelator-free modification of the PVPON$_5$-PDMS$_{30}$-PVPON$_5$ triblock copolymer nanovesicle (∼60 to 80 nm in diameter) with a polyphenol polymer layer that can be simultaneously used to anchor ^{89}Zr radiotracer (or other active metal ions) for molecular imaging and a HER2-targeting ligand Tmab for nanovesicle targeting to HER2-positive breast cancer cells. The ^{89}Zr-radiolabeled nanovesicles were analyzed *in vitro* for 7-day radiotracer retention using radio-thin layer chromatography (TLC) and *in vivo* using healthy nude mice through PET imaging and biodistribution studies. We investigated the specific targeting of ^{89}Zr-radiolabeled polymersomes to BT474 HER2-positive breast cancer cells by Tmab noncovalently anchored to the vesicle surface through hydrogen-bonded interactions with TA and found no adverse effect of these interactions on the specific binding affinity of Tmab to HER2 receptors on the cell membrane.

To the best of our knowledge, our work represents the first example of a chelator-free-radiolabeled polymersome capable of a long-term multiday PET imaging study *in vivo*. The radiolabeling approach developed herein can potentially provide stable binding of a wide spectrum of isotopes without radiometal leaching from the vesicle membrane *in vivo*. Notably, this approach integrates the inherent advantages of a polyphenolic polymersome membrane with the benefit of quickly anchoring breast cancer cell targeting ligands. In addition, the demonstrated polymer nanovesicles embody an advanced theranostic delivery vehicle with PET imaging capabilities that can be potentially extended to MRI or PET/MRI combined image-guided capability.

■ MATERIALS AND METHODS

Materials. 2,2′-Azobis(2-methylpropionitrile) (AIBN; Sigma-Aldrich) was purified by recrystallization from methanol before use. *N*-Vinylpyrrolidone (VPON; Sigma-Aldrich) and tetrahydrofuran (THF; Fisher Scientific) were distilled before use. Potassium ethyl xanthogenate (Alfa Aesar) was recrystallized before use. Diethoxydimethylsilane, 2-bromopropionyl bromide, sodium bicarbonate ($NaHCO_3$), tannic acid (TA), poly(*N*-vinylpyrrolidone) (PVPON; M_w 10 kDa), diethyl ether, ethanol anhydrous, methanol, hydrochloric acid (HCl), sodium hydroxide (NaOH), sodium sulfate anhydrous (Na_2SO_4), acetonitrile anhydrous, calcium sulfate, dialysis tubing (MWCO 2 kDa, Fisher Scientific), and dialysis Float-a-Lyzer (MWCO 300 kDa, Fisher Scientific) were used as received. 1,3-Bis(4-hydroxybutyl)tetramethyl disiloxane was purchased from Gelest, Inc. Trastuzumab (Tmab) was purchased from Genentech, Inc. Ultrapure deionized water (DI) with a resistivity of 18.2 Ω cm (Evoqua) was used for aqueous polymer and buffer solutions.

Synthesis of Bis(hydroxyalkyl) Poly(dimethylsiloxane) $PDMS_{30}$ and X-$PDMS_{30}$-X Macroinitiators. Bis(hydroxyalkyl) $PDMS_{30}$ was synthesized *via* condensation polymerization with the diethoxydimethylsilane/1,3-bis(4-hydroxybutyl)tetramethyl disiloxane molar ratio of 30:1.[60] For that, 5 g of 1,3-bis(4-hydroxybutyl)-tetramethyl disiloxane (0.018 mol), 65.7 g (0.54 mol) of diethoxydimethylsilane, 10 g of DI H_2O, and 1.2 mL of concentrated HCl (12 M) were mixed and refluxed in a flask at 60 °C for 1 h. Ethanol generated during the reaction was distilled with 42 mL of ethanol collected. Forty-two milliliters of 6 M HCl was added to the reaction flask and the content was refluxed for 4 h. The crude product (bottom layer) was separated from the aqueous phase (top layer) using a separatory funnel and dissolved in diethyl ether. The ether solution was washed with 1 M $NaHCO_3$ solution followed by DI water until neutral pH was reached. $PDMS_{30}$ was recovered from the ether by rotary evaporation followed by drying under a vacuum. The $PDMS_{30}$ was washed with a methanol/water mixture (weight ratio 75:25) under slow stirring to remove lower molecular weight fractions, including cyclic compounds. $PDMS_{30}$ was dried in a vacuum oven at 60 °C and used for macroinitiator synthesis. For the $PDMS_{30}$ macroinitiator, $PDMS_{30}$ (4 g, 2 mmol) and pyridine (2 mL, 25 mmol) were combined with diethyl ether (180 mL) in a round-bottom flask in an ice bath, and 2-bromopropionyl bromide (2 mL, 19 mmol) mixed with 20 mL of diethyl ether was added dropwise within 1 h using an addition funnel and continuous stirring. After adding the 2-bromopropionyl bromide solution, the flask was covered with a foil, and the reaction was left to run for 24 h to yield Br-$PDMS_{30}$-Br. Upon completion of the reaction, the precipitate was filtered and Br-$PDMS_{30}$-Br was recovered by extraction using 1 M solutions of HCl first and then NaOH, followed by rinsing with brine and drying over Na_2SO_4 for 2 h. Diethyl ether was removed using a rotary evaporator and the final product Br-$PDMS_{30}$-Br was dried under high vacuum. Then, Br-$PDMS_{30}$-Br (2 g, 1 mmol) and pyridine (1 mL, 12 mmol) were mixed in acetonitrile (80 mL), and potassium ethyl xanthogenate (0.8 g, 5 mmol) mixed with 20 mL of acetonitrile was added dropwise with a pipet and reacted at room temperature for 24 h to yield $PDMS_{30}$ macroinitiator (X-$PDMS_{30}$-X). Acetonitrile was evaporated using a rotary evaporator, and the macroinitiator was redissolved in diethyl ether (200 mL). The precipitate was removed by filtration, and X-$PDMS_{30}$-X was recovered by extraction, followed by solvent removal and drying under a high vacuum as described above for Br-$PDMS_{30}$-Br.

Synthesis of the $PVPON_5$-$PDMS_{30}$-$PVPON_5$ Triblock Copolymer. $PVPON_5$-$PDMS_{30}$-$PVPON_5$ triblock copolymer was synthesized by reversible addition−fragmentation chain transfer (RAFT) polymerization, as described in our earlier work.[35] For $PVPON_5$-$PDMS_{30}$-$PVPON_5$ synthesis, $PDMS_{30}$ macroinitiator (X-$PDMS_{30}$-X, 1 g, 0.5 mmol), AIBN (50 mg, 0.3 mmol), VPON (3.5 g, 32 mmol), and THF (6 mL) were added into a 25 mL Schlenk flask and degassed by a freeze−pump−thaw cycle three times. The polymerization was run at 65 °C in an oil bath for 90 min under an argon gas atmosphere. Using dialysis tubing with a 2 kDa MWCO, the reaction mixture was dialyzed in methanol for 3 days. The $PVPON_5$-$PDMS_{30}$-$PVPON_5$ polymer was recovered using a rotary evaporator, followed by drying in a vacuum oven for 24 h at room temperature. Nuclear magnetic resonance (^{1}H NMR, Bruker; 600 MHz) spectra of the polymers (10 mg mL^{-1}) were collected in $CDCl_3$ at room temperature and corrected relative to the residual solvent resonance. The number-average molecular weight of OH-PDMS-OH was calculated from ^{1}H NMR analysis based on the ratio between the integrals at δ = 0−0.2 ppm ($-SiC\underline{H}_3-$ protons in the PDMS block) and δ = 0.6 ppm ($-C\underline{H}_2O-$ protons from the end groups of PDMS). NMR analysis verified the presence of the $-C\underline{H}(CH_3)Br$ group at δ = 4.5 ppm. Using NMR analysis, we found that 95% of PDMS hydroxyl groups were converted into the bromide groups followed by 98% conversion of the former to the xanthate end groups (Figures S1−S4). The average PVPON block length was calculated from ^{1}H NMR analysis based on half of the ratio between the integrals at δ = 2.1−2.4 ppm ($-C\underline{H}_2CO-$ protons from the lactam ring of PVPON) and δ = 0.6 ppm ($-C\underline{H}_2O-$ protons from the end groups of PDMS).

Gel Permeation Chromatography (GPC). The molecular weights of OH-$PDMS_{30}$-OH and $PVPON_5$-$PDMS_{30}$-$PVPON_5$ polymers and polymer dispersity ($Đ$) were determined by GPC using pure THF as eluent. Measurements were performed on Waters 1525 system equipped with a Waters 2414 refractive index detector and Waters in-line degasser AF. Polymer solutions were prepared at a concentration of 2 mg mL^{-1} and separated using a set of two PSS SDV (5 μm; 100 000 Å; exclusion limits from 1000 to 1 000 000 Da) and a precolumn PSS SDV (5 μm) column (PSS-polymer) at a flow rate of 1 mL min^{-1} at 30 °C of the column and 35 °C of the detector. Narrow poly(styrene) standards with molecular weights within a range of 1000−187 000 Da (PSS-polymer) were used to calibrate the GPC columns. Weight-average (M_w) molecular weights were evaluated using the Breeze 2 software (Waters). By analyzing GPC traces of polymers (Figure S5), M_w of the polymers were found as 1900 Da ($Đ$ = 1.6) for OH-$PDMS_{30}$-OH and 2800 Da ($Đ$ = 1.3) for $PVPON_5$-$PDMS_{30}$-$PVPON_5$.

Self-Assembly of $PVPON_5$-$PDMS_{30}$-$PVPON_5$ Triblock Copolymer Vesicles. Polymer nanovesicles of $PVPON_5$-$PDMS_{30}$-$PVPON_5$ (PPP vesicles) were prepared using a nanoprecipitation method, as we reported earlier.[33,35] For that, 1 mL of the block copolymer solution in ethanol (5 mg mL^{-1}) was added dropwise to 4 mL of DI water at room temperature and left under stirring for 6 h, followed by dialysis in DI water for 48 h using a Float-a-Lyzer (MWCO 300 kDa, Fisher Scientific) to remove ethanol. For coating of the vesicle shell with TA, 50 μL of TA aqueous solution (4 mg mL^{-1}) was injected into 1 mL of $PVPON_5$-$PDMS_{30}$-$PVPON_5$ vesicle solution (1 mg mL^{-1}), and the mixture was shaken at 70 rpm for 15 min to form hydrogen bonds between PVPON blocks and TA. After that, excess TA was removed by dialysis in a Float-a-Lyzer (MWCO 300 kDa) against DI water for 72 h. For coating of the TA($PVPON_5$-$PDMS_{30}$-$PVPON_5$) vesicles (TA-PPP) with PVPON (M_w 10 kDa) or Trastuzumab, 50 μL of PVPON or Trastuzumab aqueous solution (4 mg mL^{-1}) was injected into 1 mL of TA-PPP vesicle solution (1 mg mL^{-1}), and the mixture was shaken at 70 rpm for 15 min. After that, an excess of PVPON or Trastuzumab was removed by dialysis in a Float-a-Lyzer (MWCO 300 kDa) against DI water for 72 h.

Dynamic Light Scattering (DLS). The hydrodynamic diameter of PPP vesicles before and after modification with TA, PVPON/TA, and Tmab was measured using a Nano-ZS Zetasizer (Malvern Pananalytical) equipped with a He−Ne laser (663 nm). The aqueous vesicle solution (1 mL; (394 ± 24) × 10^7 particles mL^{-1}) was

https://doi.org/10.1021/acs.biomac.2c01539
Biomacromolecules 2023, 24, 1784−1797

incubated at 25 °C for 24 h, transferred into a 2.5 mL four clear sided disposable fluorescence cuvette (Fisher Scientific) and capped. After a 2 min sample equilibration at 25 °C, the average vesicle diameter was obtained from three measurements (13 runs each). After size measurements, each sample was transferred to a disposable folded capillary ζ cell (Malvern Pananalytical) and an average ζ potential of each sample was obtained from three measurements (13 runs). To examine the size stability of Tmab-PPP polymersomes in serum media, the polymersomes were dialyzed in fetal bovine serum media (35-015-CV, Corning) at room temperature for 16 h using dialysis devices (Float-a-Lyzer G2 Dialysis Device, Fisher Scientific) with 1000 kDa MWCO. After dialysis, 0.3 mL of the sample was diluted to 0.9 mL with the serum and an average hydrodynamic diameter of the vesicles was measured at 25 and 37 °C with a 5 min equilibration for each temperature.

Transmission Electron Microscopy (TEM). TEM images of $PVPON_5$-$PDMS_{30}$-$PVPON_5$ (PPP), TA($PVPON_5$-$PDMS_{30}$-$PVPON_5$) (TA-PPP), and Tmab($PVPON_5$-$PDMS_{30}$-$PVPON_5$) (Tmab-PPP) vesicles were obtained using FEI Tecnai T12 Spirit TWIN TEM microscope operated at 80 kV. For that, 7 μL of each vesicle solution was dropped onto an argon plasma-treated Formvar/carbon-coated copper grid (200 mesh, Ted Pella). The adsorbed vesicles were stained with 1 wt % uranyl acetate for 30 s after blotting the excess solution.

Radio-Thin Layer Chromatography (Radio-TLC). The ^{89}Zr oxalate was prepared by the UAB Cyclotron Facility according to a previously published procedure.[61] A radio-TLC scanner (Eckert & Ziegler AR-2000) was used for direct ^{89}Zr quantification. To analyze retention of the radioisotope by the samples, 100 μL of PPP and TA-PPP vesicle solutions were combined with ~100 μCi of neutralized ^{89}Zr oxalate and incubated at 37 °C for 1 h. After 1 h, 5 μL of 50 mM DTPA (final concentration = 2.2 mM DTPA) was added to compete with the ^{89}Zr−TA complex to determine the stability of ^{89}Zr binding. Samples were taken at 1, 4, 24, 72, and 168 h after DTPA addition. The aliquots were analyzed by instant Radio-TLC to determine radiolabeling efficiency. The samples were spotted on silica iTLC plates with a 10 mM DTPA mobile phase until the solvent reached 1 cm from the top of the plate. Each sample was counted for 1 min over the entire length of the plate to accumulate sufficient counts from the scanner. The radiation counts were quantified by the interaction of the radiation with P-10 gas (90% argon, 10% methane), and the plates were analyzed using the WinScan 3.1 software. Peaks were integrated to determine the percentage of ^{89}Zr associated with each vesicle type. No radiograph peaks were visible for any polymersomes without the ^{89}Zr oxalate addition, as the TLC scanner only detects radioactivity.

Animal Model Ethical Statement. All animal experiments were conducted in compliance with the Guidelines for the Care and Use of Research Animals established by the University of Alabama at Birmingham Institutional Animal Care and Use Committee.

Preparation of ^{89}Zr-Labeled Vesicles for *In Vivo* Studies. The ^{89}Zr-radiolabeled vesicles were prepared by incubating 1.02 mCi of ^{89}Zr (60 μL) with the vesicles at 37 °C for 1 h. The samples were spotted on silica iTLC plates as described above to determine the radiolabeling efficiency. Since our polymersomes labeled > 95% of the radiotracer, no further purification was needed to complete *in vivo* studies.

Positron Emission Tomography (PET) Biodistribution Imaging. The polymersome concentration was found to be (394 ± 24) × 10^7 particles mL^{-1} as measured by NanoSight NS300 instrument (Malvern Pananalytical). For *in vivo* biodistribution studies, healthy female BALB/c mice (5 weeks age) were injected *via* the tail vein with 100 μL of [^{89}Zr]TA-PPP vesicle solution (~100 μCi ^{89}Zr as measured *via* Capintec dose calibrator CRC-25R).[62] A control group of mice was also injected with ^{89}Zr oxalate to show the biodistribution of unbound ^{89}Zr after 24 h. Dynamic imaging for 1 h was completed for the 1 h time point whereas static PET images were acquired for 10, 15, 20, or 25 min for 4, 24, 72, and 168 h, respectively. All PET images were followed by a 5 min CT at 80 kVp. The mice for each time point (n = 4) were humanely sacrificed by cervical dislocation following anesthetization with isoflurane at 1, 4, 24, 72, or 168 h post-injection, and select organs were collected and counted using an automated gamma counter. Specific uptake for each tissue was measured with background and decay correction and expressed as percent-injected dose per gram of tissue (% ID g^{-1}) as calculated by normalization to the total radioactivity injected. A known amount of injected radioactivity was used as a standard for comparison. Biodistribution data were analyzed using Prism 8.0 software. The results were expressed as mean ± standard error. The difference between mean values and standard deviation for each experimental group was determined using the one-way analysis of variance (ANOVA) with Tukey's comparison test. In all tests, $p < 0.05$ was considered significant. PET and CT images were analyzed using Vivoquant 4.0 software. CT reconstruction was completed with the Modified Feldkamp Algorithm, while PET images were reconstructed *via* the 3D-OSEM (Ordered Subset Expectation Maximation) algorithm (24 subsets and three iterations, with attenuation, random, and decay corrections). Standard uptake values (SUVs) were calculated by the Vivoquant software using the following equation

$$\mathrm{SUV} = \frac{\text{concentration of radioactivity in organ (MBq mL}^{-1})}{\text{injected radioactivity (MBq)/mouse weight (g)}} \tag{1}$$

Cell Viability Studies. BT474 and MDA-MB-468 cells were seeded in 96-well plates as 10^4 cells per well. [^{89}Zr]TA-PPP solution was diluted with its own growth media. [^{89}Zr]TA-PPP solution aliquots of 0.1, 1, 5, and 7.5 μL were used for cell studies. The same number of cell-seeded wells and growth media alone were used as the control group. The plates were incubated at 37 °C in a 5% CO_2 atmosphere for 24, 48, and 72 h. At the end of each time point, 10 μL of MTS Assay Kit solution (ab197010, Abcam) was added to each well and incubated for 4 h under the same conditions. After 4 h, the absorbances of the wells were measured using a multiplate reader at 490 nm. Cell viability (%) was calculated as [(measured absorbance value/control absorbance value) × 100%].

Cell Binding Studies. For the cell binding study, breast cancer cells MDA-MB-468 (HER2-negative; HER2−) and BT474 (HER2-positive; HER2+) were purchased from American Type Culture Collection (Manassas, Virginia). Each cell line was maintained at 37 °C with 5% CO_2 in humidified incubators. Both cell lines were grown in Gibco's high glucose Dulbecco's modified Eagle's medium (DMEM) supplemented with 10% fetal bovine serum (FBS) and 80 μM gentamicin. BT474 media also contained 1.8 mM insulin. DMEM media, FBS, and gentamicin were purchased from Thermo Fisher (Waltham, Massachusetts), while insulin was from Millipore Sigma (Burlington, Massachusetts).

Both MDA-MB-468 and BT474 cells were seeded in 24-well plates 48 h prior to experiments at a concentration of 2.5 × 10^5 cells per well. For cell binding studies, TA-PPP, PVPON/TA-PPP, and Tmab-PPP polymersomes (120 μL) were radiolabeled with ~100 μCi of neutralized ^{89}Zr (37 °C for 1 h, 1200 rpm). Each polymersome solution (60 μL) was diluted in 10 mL of complete media for the respective cell type (n = 8 of each cell type per temperature and three standards; 0.5 mL a well). The cells were incubated for 1 h at 37 or 4 °C.

After incubation, radiolabeled media was removed, and cells were washed with ice-cold phosphate-buffered saline (PBS) in triplicate. To remove the cells, 250 μL of 1 M NaOH was added and gently shaken for 5 min. Single-well components were removed and pipetted into individual microcentrifuge tubes, followed by a 250 μL wash with PBS from the same well. All samples were analyzed on a Hidex AMG automated gamma counter to determine the amount of radioactivity in each sample. Values were normalized to the overall cellular protein amount determined by a bicinchoninic acid (BCA) assay (Thermo Fisher) to determine the % binding (activity bound) per mg of cellular protein. The labeling of the vesicles was found to be 99% for [^{89}Zr]TA-PPP, 95% for [^{89}Zr]PVPON/TA-PPP, and 98% for Tmab[^{89}Zr]-PPP vesicles that were used for cell binding experiments.

RESULTS AND DISCUSSION

Synthesis of PVPON$_5$-PDMS$_{30}$-PVPON$_5$ Vesicles and Their Modification with Trastuzumab (Tmab). To obtain polymer nanovesicles, the PVPON$_5$-PDMS$_{30}$-PVPON$_5$ triblock copolymer was synthesized using the procedure we reported earlier.[35] The PDMS macroinitiator was obtained through condensation polymerization of diethoxydimethylsilane and 1,3-bis(4-hydroxybutyl)tetramethyl disiloxane[60] (Figures 1a and S1) followed by the successive modification of the hydroxyl end groups with 2-bromopropionyl bromide (Figures 1b and S2) and potassium ethyl xanthogenate (Figures 1c and S3) to yield the PDMS$_{30}$ macroinitiator (X-PDMS$_{30}$-X). After that, the PVPON$_5$-PDMS$_{30}$-PVPON$_5$ triblock copolymer was obtained from X-PDMS$_{30}$-X by RAFT polymerization of *N*-vinylpyrrolidone (Figures 1d and S4). The number-average molecular weight of PDMS was calculated from NMR analysis (Figure S1). The weight-average molecular weights calculated from GPC analysis were found to be 1900 g mol^{-1} ($Đ$ = 1.6) for OH-PDMS$_{30}$-OH and 2800 g mol^{-1} ($Đ$ = 1.3) for PVPON$_5$-PDMS$_{30}$-PVPON$_5$ (Figure S5). By dialysis of the PVPON$_5$-PDMS$_{30}$-PVPON$_5$ block copolymer in an aqueous solution (pH ∼ 5, 60 °C), the xanthogenate end groups of the triblock copolymer were converted into hydroxyl end groups as we reported earlier (Figure 2).[35,52] Following the guidance for the block copolymer assembly into vesicular morphology when the fraction of hydrophilic mass to the total copolymer mass (f) is within 0.25−0.4,[33,35] this triblock copolymer has a hydrophilic ratio f = 0.36 and can be assembled into spherical nanovesicles (polymersomes) (Figure 2a).

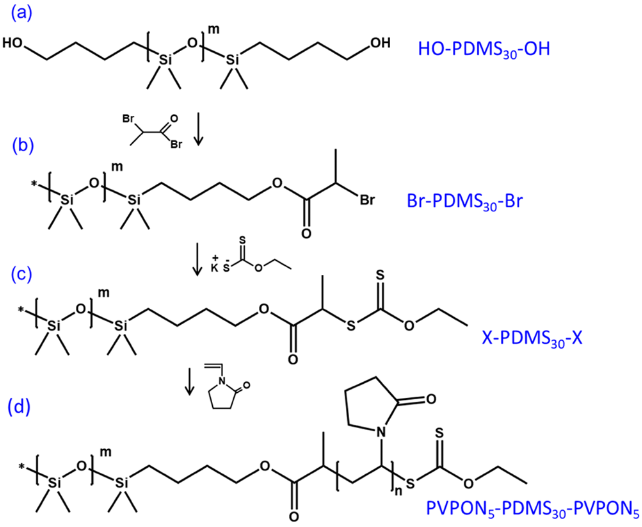

Figure 1. Synthesis of the PVPON$_5$-PDMS$_{30}$-PVPON$_5$ triblock copolymer (*: mirrored chemical structure).

The PVPON$_5$-PDMS$_{30}$-PVPON$_5$ vesicles were self-assembled *via* nanoprecipitation using an ethanol solution of the triblock copolymer.[35] Polymersomes assembled from block copolymers through nanoprecipitation have been reported to typically produce a unilamellar structure and narrow size distributions.[63] In our earlier study, using small-angle neutron scattering (SANS), we demonstrated that the PVPON$_5$-PDMS$_{30}$-PVPON$_5$ copolymer assembly *via* nanoprecipitation results in a three-dimensional globule shape of the vesicle with a model fit describing a hollow sphere with a nonnegligible shell.[35] SANS analysis also confirmed no temperature-responsive changes in the polymersome shell in the temperature range from 25 to 55 °C with an average vesicle membrane thickness of 8 nm.[35]

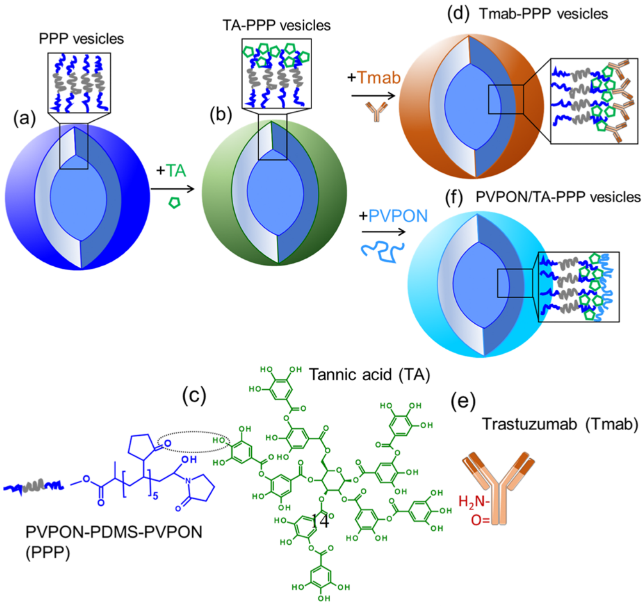

Figure 2. Assembly of (a) PVPON$_5$-PDMS$_{30}$-PVPON$_5$ vesicles and their modification with (b) TA (TA-PPP vesicles through hydrogen bonding of PVPON and TA (c)), with (d) Tmab (Tmab-PPP vesicles through hydrogen bonding and ionic pairing between TA and Tmab (e)), and (f) PVPON homopolymer (PVPON/TA-PPP vesicles).

After purification of the polymer vesicles from ethanol using dialysis in DI water, TA was adsorbed onto the vesicle surfaces from 4 mg mL^{-1} aqueous solution of TA (Figure 2b,c).[35,64] The excess TA was removed from the vesicle solution using dialysis in DI water, leaving behind TA-coated PVPON$_5$-PDMS$_{30}$-PVPON$_5$ polymer vesicles (TA-PPP, Figure 2d). The modification of the polymersome surfaces with TA serves two purposes: (1) to allow efficient radiolabeling of the vesicles with a highly stable positron-emitting isotope, ^{89}Zr, for a multiday *in vivo* imaging of the vesicles and (2) to permit a simple and quick modification of the vesicles with targeting ligands, such as trastuzumab (Tmab). The latter can be possible because of strong interactions of TA with protein molecules through hydrogen bonding between carbonyl and amine moieties of the peptide bond and hydroxyl groups of TA.[65−68] The formation of the TA−Tmab water-insoluble intermolecular complex was confirmed in the turbidity measurements using UV−visible spectroscopy of TA, Tmab, and TA−Tmab aqueous solutions at 400 nm (Figure S6). The TA−Tmab interaction is due to the formation of hydrogen bonds between carbonyl groups in Tmab and hydroxyl groups of TA and ionic pairing between amine groups of Tmab and partially ionized hydroxyl groups of TA (Figure 2e).

The interaction of TA with amine-containing polyelectrolytes has been previously demonstrated to produce water-insoluble intermolecular complexes stable at physiological conditions.[69,70] Moreover, we have recently shown that adsorbing chicken ovalbumin onto the outer TA layer of (PVPON/TA)$_4$ multilayer microcapsules allowed for the targeting of hyperinflammatory macrophages to antigen-specific T cells.[55] The noncovalent anchoring of targeting protein molecules with the nanovesicle membrane may prove highly advantageous compared to currently developed covalent

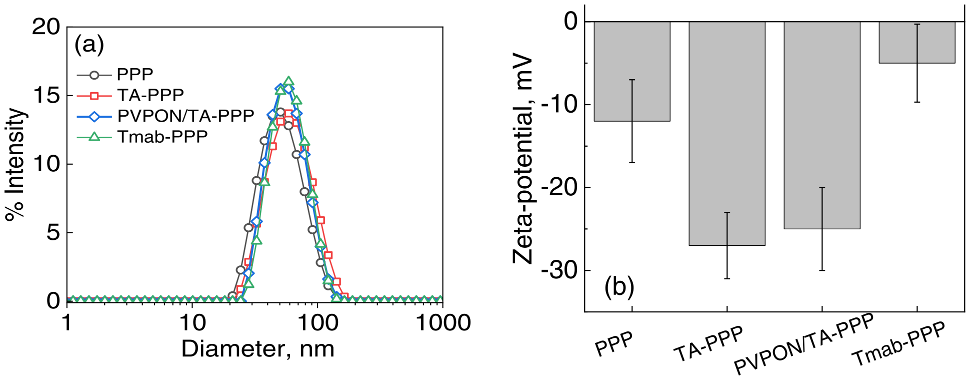

Figure 3. (a) Hydrodynamic diameters of the PPP vesicles before modification (circles), and after subsequent modification with TA (TA-PPP; squares) and PVPON (PVPON/TA-PPP; rhombus) and after Tmab adsorption onto TA-PPP vesicles (Tmab-PPP vesicles; triangles). (b) ζ-Potential measurements of PPP, TA-PPP, PVPON/TA-PPP, and Tmab-PPP vesicles.

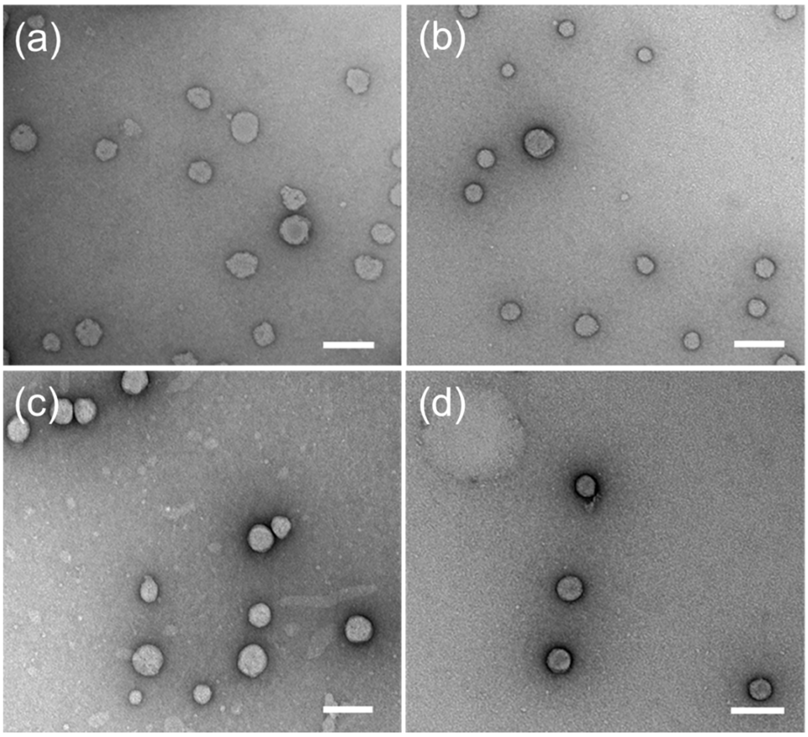

Figure 4. TEM images of (a) PPP vesicles, (b) TA-PPP vesicles, (c) PVPON/TA-PPP vesicles, and (d) Tmab-PPP vesicles. The scale bar is 100 nm in all images.

methods as it will allow for easy and quick integration of a broad range of targeting ligands to the vesicle surface. Therefore, to induce TA-PPP with breast cancer cell targeting function, Tmab was adsorbed onto surfaces of TA-PPP vesicles from 4 mg mL^{-1} of the monoclonal antibody solution, and free, nonadsorbed Tmab was then dialyzed off the solution in DI water (Figure 2d,e). As a nontargeting negative control, TA-PPP vesicles coated with a layer of PVPON with M_w of 10 kDa instead of Tmab were also obtained and denoted as PVPON/TA-PPP (Figure 2f). The PVPON adsorption onto TA-coated PPP vesicles was carried out in a dialysis tube (a Float-a-lyzer), and nonadsorbed PVPON was removed from the vesicle solution *via* dialysis in DI water.

The average hydrodynamic diameter of the PPP vesicles was measured by DLS to be 60 ± 25 nm (Figure 3a, circles) and did not significantly change after the interaction of the PVPON corona on the PPP vesicles with TA. Thus, using DLS, the average hydrodynamic size of TA-PPP vesicles was measured as 65 ± 25 nm (Figure 3a, squares). Interestingly, TA adsorption onto the PPP vesicle surfaces also decreased the particle net surface charge. Thus, the surface charge of PPP vesicles before TA adsorption was only slightly negative with the ζ-potential value of −12 ± 5 mV (Figure 3b), which agrees with the reported negative ζ potential values of untreated PDMS in the range from −57 to −88 mV at neutral pH.[71] A lower value of the ζ potential observed for the PPP vesicles herein can be due to the shielding of PDMS blocks with PVPON outer blocks, which shifted the effective shear plane where the electrophoretic mobility is measured away from the polymer nanovesicle membrane due to hydrodynamic immobilization of water associated with the polymer loops.[72] After TA binding to PVPON outer blocks on the PPP vesicles, the resultant TA-PPP polymer vesicles demonstrated a ~2-fold decrease in the average ζ-potential value from −12 ± 5 to −27

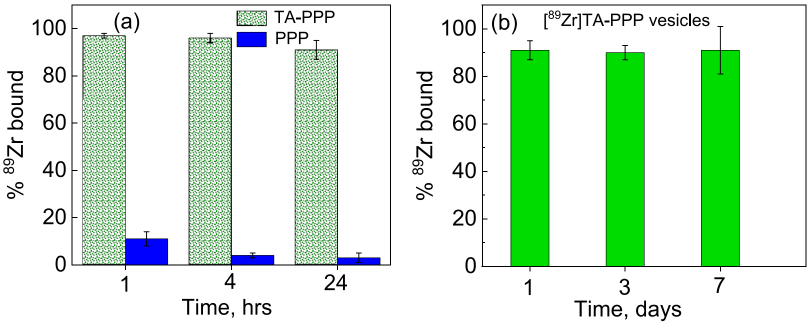

Figure 5. Radio-TLC analysis of (a) PPP and TA-PPP vesicles after 1, 4, and 24 h after exposure to ^{89}Zr oxalate solution and (b) TA-PPP vesicles after 1, 3, and 7 days after exposure to ^{89}Zr oxalate solution.

± 4 mV (Figure 3b). The observed surface charge decrease is due to partial TA ionization at the vesicle solution pH of 5.4−5.6, as TA has pK_a in the range of 5−6.[73]

It is worth noting that we did not observe any decrease in the TA-PPP vesicle size after TA adsorption that would be expected upon the formation of hydrogen bonds between TA and PVPON. Thus, for example, as reported earlier,[64] hydrogen bonding of TA with the PVPON corona of PVCL$_{179}$-*b*-PVPON$_{205}$ diblock copolymer polymersomes at 50 °C led to the size decrease of the obtained polymersomes from 770 to 250 nm. The polymersome size decrease, however, was dependent on the initial size of PVCL-*b*-PVPON polymersomes, with the initially smaller vesicles shrinking to a lesser extent than the larger ones. For example, the 250-nm-sized PVCL$_{179}$-*b*-PVPON$_{234}$ diblock copolymer vesicles shrank to only 190 nm in diameter upon interacting with TA.[64] Apparently, the initially smaller size of PVPON$_5$-PDMS$_{30}$-PVPON$_5$ polymersomes used in this work (60 ± 25 nm) did not facilitate any further particle size decrease.

In contrast, when Tmab was adsorbed onto TA-modified vesicle surfaces, the net surface charge of the Tmab-PPP vesicles increased to a slightly negative ζ-potential value of −5 ± 4 mV (Figure 3b). The observed drastic increase in the surface charge of Tmab-PPP polymer nanovesicles can be explained by charge neutralization at the surface of the protein−TA complexes either *via* electrostatic or hydrogen bonding interactions. This result agrees with the reported electrostatic properties of Tmab, which has an isoelectric point of ∼8.8 and is shown to have a slightly positive net molecular charge of +3.3 ± 0.3 mV at pH = 7.5 (0.15 M NaCl).[74] Conversely, upon adsorption of PVPON on top of TA-PPP vesicles, the net surface charge of the PVPON/TA-PPP vesicles decreased slightly with the average zeta-potential of −25 ± 5 mV (Figure 3b). Notably, the average hydrodynamic size of Tmab-PPP (60 ± 18 nm) and PVPON/TA-PPP (60 ± 20 nm) vesicles did not increase and remained similar to that of the initial PPP and TA-PPP vesicles, indicating excellent colloidal stability of the modified nanovesicles. The negative charge on particle surfaces was previously shown to be beneficial for *in vivo* use as anionic particles demonstrated low systemic immune response and cytotoxicity.[75] Indeed, the Tmab-PPP vesicles demonstrated good stability in serum solution. An average hydrodynamic size of Tmab-PPP vesicles assembled in water at 25 °C did not show significant changes at 25 or 37 °C after exposure to fetal bovine serum for 16 h as measured by DLS (Figure S7).

TEM analysis of four types of the polymersomes in Figure 4 demonstrated the presence of intact nanoparticles at all stages of modification. TEM images show that after the surface modification of PPP vesicles (Figure 4a) with TA (Figure 4b), PVPON/TA (Figure 4c), and Tmab/TA (Figure 4d), their shape did not change and there were no signs of vesicle fusion, indicating their structural integrity upon modification. The average size of the dry vesicles remained smaller than 100 nm, which agrees with our DLS data (Figure 3a).

Radiolabeling of PPP, TA-PPP, and Tmab-PPP Polymersomes. As TA can bind metal ions through nonspecific ionic pairing,[76] we, therefore, used it to bind ^{89}Zr^{4+} radioisotope ions to TA-PPP vesicles (Figure 5a). In our recent work on multilayer capsules made *via* layer-by-layer assembly of TA and PVPON, we have demonstrated the binding of the ^{89}Zr radiotracer to the TA-containing capsule wall with the radiolabeling yield of 69% after 24 h.[77] In contrast to a micrometer-sized multilayer capsule wall of 25−50 nm made of several layers of TA shielded by PVPON layers through hydrogen bonding, radiolabeling of an 8-nm-thick vesicle membrane[35] coated with a single TA layer can be challenging with an uncertain fate of the radiotracer during long-term retention by the vesicle membrane.

Herein, we have developed the vesicle labeling procedure and investigated the efficiency of the ^{89}Zr labeling as well as the ^{89}Zr retention within the ^{89}Zr^{4+}−TA complex inside the vesicle nanothick shell. To determine the radiolabeling efficiency, both PPP and TA-PPP polymersome solutions were incubated with a solution of [^{89}Zr]Zr oxalate (∼100 μCi) at 37 °C for 1 h to enable interaction of the TA outer layer and the radioisotope. After polymersome labeling, the ^{89}Zr-treated vesicles were analyzed by radio-TLC (Figure S8). Radiolabeling yield was quantified by integrating the peak areas on a radio-TLC plate, and the relative peak percent representing the percentage of ^{89}Zr bound to a vesicle shell was compared between PPP and TA-PPP polymersomes after 1, 4, and 24 h of exposure.

Figure 5 demonstrates a dramatic difference in the radiotracer binding to TA-PPP vesicles compared to the unmodified PPP vesicles. After 1 h of radionuclide exposure, the radiolabeling yields were found to be 97 ± 1 and 11 ± 3% for TA-PPP and PPP polymersomes, respectively (Figure 5a). The percentage of ^{89}Zr bound to the vesicle shell only slightly decreased to 96 ± 2 and 91 ± 4% after 4 and 24 h of incubation for TA-PPP vesicles, while the radiotracer was almost completely released from the bare PPP shell with the corresponding values of bound ^{89}Zr being 4 ± 1 and 3 ± 2%, after 4 and 24 h (Figure 5a). The initial binding of ^{89}Zr^{4+} to PPP vesicles can be due to the isotope's initial coordination with hydroxyl end groups and carbonyl groups[78] on PVPON blocks of the PPP shell, with these interactions, obviously, not sufficiently strong for long-term retention of the metal ions. In contrast, [^{89}Zr]TA-PPP vesicles demonstrated a highly stable binding of ^{89}Zr to the vesicle shell. Figure 5b shows that the radiochemical yield remained consistent after the labeling over 1, 3, and 7 days of observation, with the corresponding values of bound ^{89}Zr being 91 ± 4, 90 ± 3, and 91 ± 10%. Indeed, Zr^{4+}−TA coordination complexes in metal-phenolic networks were demonstrated to be highly stable in the pH range from 5 to 7[76,79] due to the formation of tris complexes of zirconium ions with TA.[80]

In the case of Tmab adsorbed as the outer layer on the TA-PPP vesicles to obtain Tmab-PPP polymersomes, one might expect a decreased radiolabeling efficiency of the TA layer due to TA interaction with Tmab, and possible electrostatic repulsions between the amine groups of Tmab molecules and $^{89}Zr^{4+}$ ions. Despite that, radio-TLC analysis of Tmab-PPP polymersomes after incubation with ^{89}Zr showed high binding efficiency of the radiotracer to the vesicles. Figure 6 demonstrates that the radiochemical yield of 97 ± 3% was achieved after 1 h of incubation and remained stable for at least 168 h (7 days) of observation with the percentage of ^{89}Zr-bound value of 92 ± 6% at the final time point for Tmab[^{89}Zr]TA-PPP nanovesicles, which is similar to that found for [^{89}Zr]TA-PPP vesicles (91 ± 10%) after 168 h of incubation.

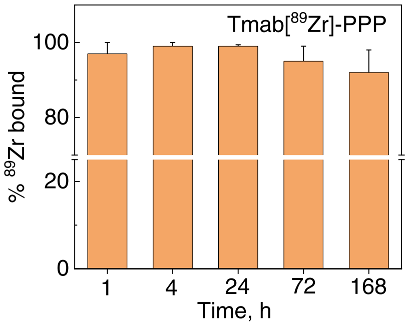

Figure 6. Radiolabeling (% ^{89}Zr bound) of Tmab-PPP vesicles analyzed as Tmab[^{89}Zr]-PPP vesicles by radio-TLC.

Our ^{89}Zr binding data indicates much faster and more efficient radiolabeling of the TA and Tmab-modified PPP vesicles compared to TA/PVPON multilayer capsules demonstrated earlier.[77] Thus, for example, the radiolabeling yield of [^{89}Zr](TA/PVPON) multilayer capsules with six layers of TA slowly increased from 22 to 69% after 1 and 24 h, respectively.[77] A similar trend was found for the multilayer capsules assembled from TA and a PVPON copolymer containing monomer units functionalized with deferoxamine (PVPON-DFO), where the presence of DFO led to a 17% increase in the radiolabeling efficiency of the multilayer capsules.[77] However, the radiolabeling efficiency of TA/PVPON-DFO microcapsules was still lower (89%) after 24 h compared to that of the TA-PPP (∼91%) and Tmab-PPP (∼92%) block copolymer vesicles in this work.

In another work, PEGylated liposomal vesicles assembled with a folate-cholesterol amphiphile demonstrated a lower radiochemical yield of 78%, which could be later increased to 98% by introducing a DFO chelator.[50] Also, increasing the incubation time of a radionuclide with glucose-modified liposomes from 15 to 60 min was previously shown to increase the labeling efficiency of liposomal vesicles with ^{177}Lu from 78 to 97%.[81] However, much lower radiolabeling efficiencies of ∼49% have been reported for polymersomes assembled from amphiphilic poly(butadiene)-*b*-poly(ethyleneoxide) diblock copolymers and radiolabeled with ^{213}Bi.[44] Therefore, the TA-modified PPP polymersomes demonstrated herein showed an excellent ^{89}Zr radionuclide binding and stability and can be a simple and facile way to achieve it, unlike previous reports.

We also confirmed the radiolabeling stabilities of [^{89}Zr]TA-PPP and Tmab[^{89}Zr]-PPP vesicles after their exposure to human serum for 1, 4, 24, 72, 120, and 168 h. The percentage of the vesicles intact after human serum exposure was analyzed using radio-TLC at 1, 4, 24, 72, 120, and 168 h to determine the amount of breakdown products (free or released radiotracer) in each sample (Figure S9). In both types of

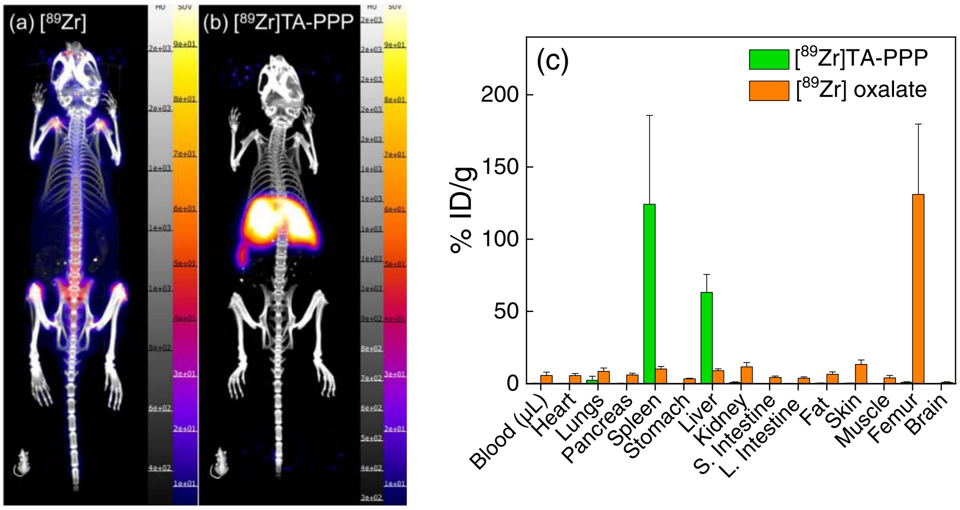

Figure 7. (a, b) Representative maximum projection PET images (maximum intensity projections) of healthy BALB/c mice ($n = 4$) 24 h after injection of (a) free ^{89}Zr isotope (^{89}Zr oxalate) and (b) [^{89}Zr]TA-PPP vesicles. SUV scale is 1−100 in both images. (c) Biodistribution of [^{89}Zr]TA-PPP vesicles and free ^{89}Zr isotope (^{89}Zr oxalate) in BALB/c mice 24 h after injection ($n = 4$). Values are presented as average % ID g^{-1} ± standard errors.

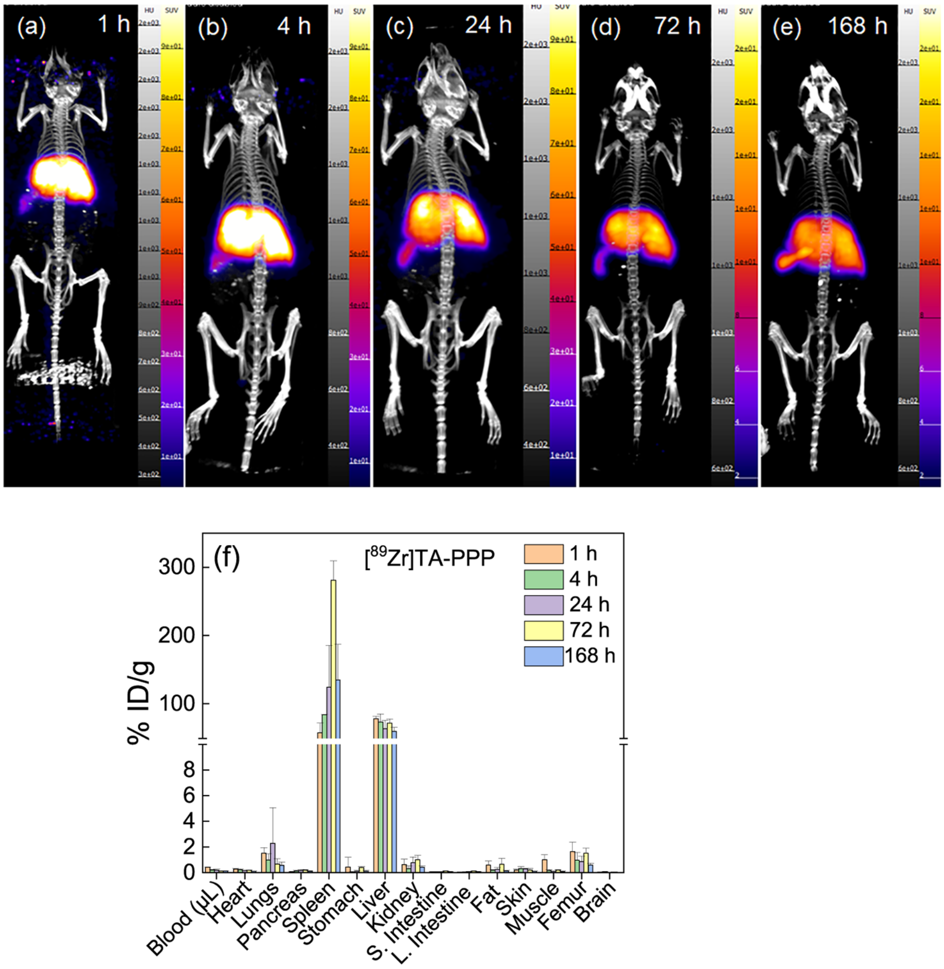

Figure 8. (a−e) Representative PET images (maximum intensity projections) of healthy BALB/c mice (n = 4) at (a) 1 h, (b) 4 h, (c) 24 h, (d) 72 h, and (e) 168 h after injection of [^{89}Zr]TA-PPP vesicles. SUV scale is (a−c) 1−100 and (d, e) 1−20. (f) Biodistribution of [^{89}Zr]TA-PPP vesicles in BALB/c mice at 1, 4, 24, 72, and 168 h after injection (n = 4). Values are presented as average % ID g^{-1} ± standard errors.

polymersomes, the radiolabeling was highly stable after 1 h of serum exposure with 98 ± 1 and 92 ± 3% of intact vesicles for [^{89}Zr]TA-PPP and Tmab[^{89}Zr]-PPP, respectively (Figure S10). After 168 h of serum exposure, the radiolabeling stability did not significantly change for the [^{89}Zr]TA-PPP vesicles (97 ± 1% of intact vesicles) while decreasing to that of 84 ± 2% for the Tmab[^{89}Zr]-PPP vesicles after 72 h of serum exposure and being stable at that value after 168 h of serum exposure (84 ± 1%) (Figure S10).

Importantly, radiolabeling of TA-PPP vesicles did not exhibit any cytotoxicity as observed for [^{89}Zr]TA-PPP polymersomes incubated with BT474 and MDA-MB-468 cancer cells for 24, 48, and 72 h (Figure S11). The viability of the cells at varied concentrations of the vesicles was found more than 90% after 3 days of incubation with no significant differences observed between the cell groups. These results also agree with our previous reports on nontoxicity of PVPON and PVPON/TA polymer materials.[52−58]

In Vivo PET Imaging of [^{89}Zr]-Labeled PPP Vesicles.

Since the binding stability of ^{89}Zr in [^{89}Zr]TA-PPP vesicles *in situ* discussed above is sufficiently high for clinical use, we explored the stability of the radiotracer within the vesicle shell *in vivo*. We carried out *in vivo* imaging studies of healthy BALB/c mice (n = 4) after their injection with an average of 100 μCi dose from free ^{89}Zr isotope (from ^{89}Zr oxalate) or from [^{89}Zr]TA-PPP vesicles. Healthy mice were chosen as a model to determine how the healthy immune response would influence the circulation of the [^{89}Zr]TA-PPP vesicles in a body and affect the imaging contrast. The mice were injected *via* tail vein with either the free radiotracer or labeled [^{89}Zr]TA-PPP polymersomes and then imaged with PET at 1, 4, 24, 78, and 168 h after injection. The biodistribution of the vesicles within the main body organs was analyzed after each respective time point after humanely sacrificing mice and assaying the body organs for radioactivity. It is important to note that strong *in vivo* retention of ^{89}Zr tracer within the polymersome membrane is especially important as that would allow tracing the fate of the vesicles *in vivo* and an easy control by PET over the delivery of therapeutics in the clinical environment.

PET images in Figure 7 demonstrate a strong imaging contrast in both samples after 24 h of study. The biodistribution of the free ^{89}Zr radionuclide from the metal oxalate has been previously reported to localize largely in the spine and femur in animal biodistribution models due to chelation by phosphate constituents of bones.[82−84] In fact, a pronounced PET signal is seen in the mouse spine and hips with a strong articulation in the knees (Figure 7a), while an excellent imaging contrast is observed in the liver and spleen for the [^{89}Zr]TA-PPP vesicles (Figure 7b). Analysis of the

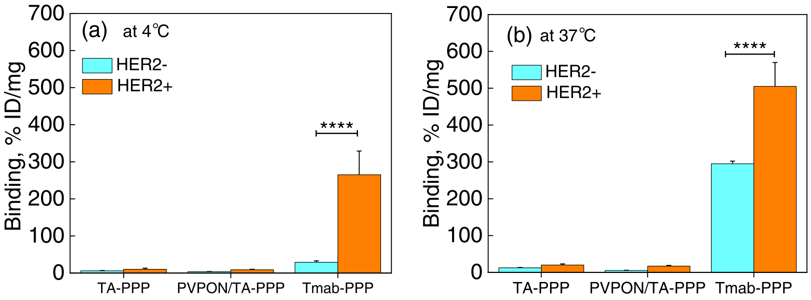

Figure 9. Binding (% ID mg^{-1} of cellular protein) of ^{89}Zr-radiolabeled TA-PPP, PVPON/TA-PPP, and Tmab-PPP vesicles to HER2− and HER2+ cells at (a) 4 °C and (b) 37 °C (****$p < 0.0001$).

bone uptake, as the percent-injected dose per gram of tissue (% ID g^{-1}) as calculated by normalization to the total radioactivity injected, shows that femur uptake was indeed high (131 ± 48% ID g^{-1}) for the free noncomplexed ^{89}Zr (Figure 7a,c) after 24 h, while it was negligible in bone for the labeled vesicles at this time point (0.9 ± 0.4% ID g^{-1}) (Figure 7b,c). The observed drastic difference between the biodistribution of the free ^{89}Zr and the metal radiotracer-labeled vesicle is important as it demonstrates an unimpeded capability of the polymeric nanocarrier to be tracked *in vivo*. In this regard, using the ^{89}Zr radiotracer is advantageous compared to other radionuclides. For example, the free ^{64}Cu radioisotope is known to accumulate commonly in the liver[85] and can be easily mistaken for the ^{64}Cu-labeled carrier in the case of ^{64}Cu weak binding to a delivery vehicle and a possible release of the tracer from the drug carrier.[76]

Excellent retention of the radiotracer in the [^{89}Zr]TA-PPP vesicle shell was further evidenced using PET imaging of the mice for longer times. The PET images in Figure 8 show that a strong imaging contrast can be observed at the final time point of 168 h (7 days) of the imaging study. Note that a good imaging contrast can be observed at much lower activity in Figure 8d,e where the standardized uptake value (SUV) scale is 1−20, unlike that of 1−100 in Figure 7a−c. The PET images do not show any imaging contrast from the bone, implying an overall strong attachment of the radiotracer to TA in the TA-PPP polymersome shell. Indeed, the bone (femur) uptake was found to be less than 1% ID g^{-1} in the mice after 7 days, confirming excellent retention of ^{89}Zr−TA complexes in the [^{89}Zr]TA-PPP vesicle shell (Figure 8f). These results agree with our previous study, where the biodistribution of 4-μm-sized TA-containing multilayer capsules in the femur for healthy mice reached 4 ± 2% ID g^{-1} after 7 days of observation.[77] The absence of radioactive bone uptake in the case of the [^{89}Zr]TA-PPP vesicle illustrates a superior radiolabeling method compared to the chelator-free radiolabeling of liposomes where ^{89}Zr was directly coordinated by phosphate heads of phospholipid membranes.[50] Bone accumulation in those liposomes reached up to 12% ID g^{-1} due to the release of free ^{89}Zr after 50 h post-injection.[50] Moreover, radionuclide retention by TA-PPP polymersome membrane in this work was much more robust compared to DFO chelator-based polybutadiene-*b*-poly(acrylic acid) micelles where DFO-^{89}Zr coordination still allowed for a partial release of free ^{89}Zr and, consequently, bone accumulation at 4% ID g^{-1}.[43]

Note that since the PET imaging contrast was studied *in vivo* using healthy mice, the 60-nm-sized polymersomes have been accumulating mainly in liver and spleen (Figure 8f), which is an expected clearance through the mononuclear phagocyte system typical for nanomaterials with sizes larger than 6−8 nm.[46,86−88] For example, the main accumulation sites for ~10-nm-sized ^{89}Zr-labeled lipoprotein nanoparticles were found to be in the spleen, liver, and kidneys along with tumor-associated macrophages.[89] Polybutadiene-based diblock copolymer 25 nm micelles, functionalized with ^{89}Zr-deferoxamine, have also been reported to accumulate in the liver and spleen after 120 h post-injection into tumor-bearing mice.[43]

Targeting Tmab[^{89}Zr]-PPP Vesicles *In Vitro*. We also assessed the ability of Tmab[^{89}Zr]-PPP vesicles to target HER2 receptors *in vitro* using BT474 HER2-positive (HER2+) breast cancer cells. The HER2-negative (HER2−) MDA-MB-468 cells were used as a negative control. Three types of polymersomes were labeled with [^{89}Zr]Zr oxalate with a high radiochemical yield of 99% for TA-PPP, 95% for PVPON/TA-PPP, and 98% for Tmab-PPP vesicles and then incubated with the cells for 1 h at 4 or 37 °C. Cell interaction with the polymersomes at 4 °C was performed to limit the endocytosis of HER2 receptors from the cell surface into the cell interior (HER2 internalization).

Each sample radioactivity was used to determine the percentage of cell binding (activity bound) per mg of cellular protein (% ID mg^{-1}). Binding analysis demonstrates that there was almost no binding of nontargeting [^{89}Zr]TA-PPP and [^{89}Zr]PVPON/TA-PPP vesicles to both types of HER2 cells upon cell incubation at 4 °C (Figure 9a). In contrast, Tmab-targeting vesicles (Tmab[^{89}Zr]-PPP) showed a high binding activity to the HER2-positive cells (265 ± 64% ID mg^{-1}), with only a marginal binding activity (29 ± 4% ID mg^{-1}) toward HER2-negative cancer cells (Figure 9a). This result illustrates a specific binding of the Tmab-targeting polymersomes to HER2+ receptors on the cell surface. The incubation at 4 °C promoted the decrease in the amount of HER2 recycling where HER2 is internalized after Tmab binding to the receptor and is either recycled back to the cell surface or degraded in cell lysosomes.[90] The observed binding of Tmab[^{89}Zr]-PPP vesicles to the HER2+ BT474 cells confirms that TA−Tmab complexation does not affect the specific binding affinity of Tmab to HER2 receptors on the cell membrane and can be used for specific targeting of the polymer nanovesicles to HER2 receptors.

As expected, no binding to either type of cells was observed for nontargeting TA-PPP and PVPON/TA-PPP vesicles after cell incubation at 37 °C, similar to that observed at 4 °C (Figure 9b). In contrast, we observed a ~2-fold increase in HER2 binding in HER2+ BT474 cells (505 ± 65% ID mg^{-1}) compared to that at 4 °C (265 ± 65% ID mg^{-1}). This result can possibly be explained by the internalization and rapid recycling of HER2. As reported earlier, the ability of SK-BR-3 cancer cells to rebind an antibody at 37 °C was shown to be dependent on the endocytotic dissociation of a HER2/antibody complex and HER2 recycling to the cell membrane with the initial HER2 density on the cell surface being restored only after 72 h. Conversely, upon HER2 internalization by BT474 human breast cancer cells *in vitro*, 50 and 85% of internalized Tmab-HER2 could be recycled to the cell membrane within 5 and 30 min, respectively.[90]

Interestingly, the incubation of the cells at 37 °C resulted in the binding of Tmab-PPP vesicles to MDA-MB-468 HER2-negative cells with 295 ± 7% ID mg^{-1} (Figure 9b). As recently demonstrated, Tmab treatment could decrease cell proliferation in HER2-negative breast cancer cell lines that have HER2 phosphorylation at tyrosine Y877 position of the receptor (pHER2^{Y877}+ status) to an extent comparable to what occurs in HER2+ cell lines.[91] Tmab sensitivity in HER2−/pHER2^{Y877}+ MDA-MB-468 cell line that was used in our work was shown to be specific to HER2 tyrosine 877 phosphorylation; however, it required higher Tmab doses. For instance, the decrease in the HER2−/pHER2^{Y877}+ MDA-MB-468 cell viability was found to start at 50 μg mL^{-1} of Tmab compared to that of 4 μg mL^{-1} for HER2+ cell lines.[91] Indeed, the observed binding of Tmab[^{89}Zr]-PPP vesicles to the MDA-MB-468 cells was less pronounced at 37 °C compared to that for the HER2+ BT474 cells at this temperature, and Tmab targeting of the polymer vesicles was still significantly higher by 1.7-fold at 37 °C for HER2+ cells (Figure 9b). These results from Tmab-PPP targeting polymer nanovesicles warrant further experiments *in vivo* to investigate the effect of Tmab-targeting of breast cancer tumors in HER2+ cells and in HER2-negative cell lines with pHER2^{Y877+} status such as MDA-MB-468 triple-negative breast cancer lines for which a personalized therapy is still not achieved.

■ CONCLUSIONS

We have demonstrated a simple and facile method for chelator-free radiolabeling of block copolymer vesicles with ^{89}Zr for PET imaging *in vivo*. Stable PVPON$_5$-PDMS$_{30}$-PVPON$_5$ triblock copolymer polymersomes of 60 nm diameter were assembled in an aqueous solution using the nanoprecipitation method. We showed that a layer of TA could be adsorbed on the assembled nanovesicles through hydrogen bonding of the vesicles' PVPON corona and TA without affecting the polymersome size and colloidal stability. We also demonstrated that the TA-coating could be used for a stable noncovalent anchoring of Tmab onto the TA surface through hydrogen bonding. The demonstrated noncovalent anchoring of Tmab with the polymersome membrane can be highly advantageous compared to the currently developed covalent methods, as it will allow for easy and quick integration of a broad range of targeting protein molecules to the vesicle surface. We found that, unlike bare PVPON$_5$-PDMS$_{30}$-PVPON$_5$ polymersomes, TA- and Tmab-modified polymersomes could be efficiently radiolabeled with the ^{89}Zr radiotracer with a high radiochemical yield of more than 95% through the formation of the TA−^{89}Zr complex. *In vivo* PET imaging studies demonstrated excellent retention of the ^{89}Zr in the TA shell of the vesicles for up to 7 days *in vivo*. Animal biodistribution analysis using healthy mice revealed that the majority of ^{89}Zr-labeled polymersomes accumulated in spleen and liver, with no accumulation in the femur. At the same time, the accumulation of free nonbound ^{89}Zr radiotracer observed in the femur confirms the strong retention of the radionuclide by the polymersome shell. Finally, we found that the ^{89}Zr-radiolabeled polymersomes could be used to confirm specific targeting of the vesicles to BT474 HER2-positive breast cancer cells by Tmab non-covalently anchored to the vesicle surface through hydrogen-bonded interactions with TA. The binding of Tmab[^{89}Zr]-PPP vesicles to the HER2+ BT474 cells revealed that TA−Tmab complexation did not affect the specific binding affinity of Tmab to HER2 receptors on the cell membrane. Given the previously demonstrated ability of these polymersomes to encapsulate and release anticancer therapeutics into cancer cells,[35,52] these theranostic polymersomes can be further developed as advanced precision-targeted therapeutic carriers for the advancement of human health through highly effective drug delivery strategies.

■ ASSOCIATED CONTENT

SI Supporting Information

The Supporting Information is available free of charge at https://pubs.acs.org/doi/10.1021/acs.biomac.2c01539.

> ^{1}H NMR spectra of HO-PDMS$_{30}$-OH, Br-PDMS$_{30}$-Br, and X-PDMS$_{30}$-X precursors; GPC traces of OH-PDMS$_{30}$-OH and PVPON$_5$-PDMS$_{30}$-PVPON$_5$ polymers; photograph of the TA−Tmab complex in DI water solutions and UV−vis absorbance of TA, Tmab, and TA−Tmab complex solutions; hydrodynamic diameter of Tmab-PPP vesicles at 25 and 37 °C after incubation in fetal bovine serum; representative radiographs of PPP and TA-PPP vesicles after exposure to ^{89}Zr oxalate and Tmab[^{89}Zr]-PPP vesicles after DTPA challenge; representative radiographs of ^{89}Zr-radiolabeled TA-PPP and Tmab[^{89}Zr]-PPP vesicles after exposure to human serum; radiolabeling stability of [^{89}Zr]TA-PPP and Tmab[^{89}Zr]-PPP vesicles after exposure to human serum; and cell viability of BT474 and MDA-MB-468 cells after incubation with [^{89}Zr]TA-PPP polymersomes (PDF)

■ AUTHOR INFORMATION

Corresponding Author

#Eugenia Kharlampieva − *Department of Chemistry, University of Alabama at Birmingham, Birmingham, Alabama 35294, United States; O'Neal Comprehensive Cancer Center and Center for Nanomaterials and Biointegration, University of Alabama at Birmingham, Birmingham, Alabama 35294, United States;* orcid.org/0000-0003-0227-0920; Email: ekharlam@uab.edu

Authors

Veronika Kozlovskaya − *Department of Chemistry, University of Alabama at Birmingham, Birmingham, Alabama 35294, United States;* orcid.org/0000-0001-9089-4842

Maxwell Ducharme − *Department of Radiology, University of Alabama at Birmingham, Birmingham, Alabama 35294, United States*

Maksim Dolmat − *Department of Chemistry, University of Alabama at Birmingham, Birmingham, Alabama 35294, United States;* orcid.org/0000-0002-4918-7342

James M. Omweri − *Department of Chemistry, University of Alabama at Birmingham, Birmingham, Alabama 35294, United States; Department of Radiology, University of*

Alabama at Birmingham, Birmingham, Alabama 35294, United States

Volkan Tekin – *Department of Radiology, University of Alabama at Birmingham, Birmingham, Alabama 35294, United States*

[#]**Suzanne E. Lapi** – *Department of Radiology and O'Neal Comprehensive Cancer Center, University of Alabama at Birmingham, Birmingham, Alabama 35294, United States*

Complete contact information is available at: https://pubs.acs.org/10.1021/acs.biomac.2c01539

Author Contributions

[⊥]V.K. and M.D. contributed equally.

Notes

The authors declare no competing financial interest.

[#]S.E.L. and E.K. share equal seniority.

■ ACKNOWLEDGMENTS

This work was supported by the NSF DMR Award #2208831. The authors acknowledge UAB High-Resolution Imaging Facility for TEM use. Karin Hardiman, M.D., Ph.D., and Regina Irwin, B.S. (UAB Department of Surgery) are acknowledged for technical assistance with NanoSight NS300 measurements. Dr. Pavel Nikishau (UAB Chemistry) is greatly acknowledged for technical assistance with chromatography and NMR spectroscopy. This work was also supported by the Department of Radiology at the University of Alabama at Birmingham. Imaging studies were supported by the Small Animal Imaging Core through the O'Neal Cancer Center P30CA013148. This material is in part based upon work supported under the IR/D Program by the National Science Foundation (E.K.). Any opinion, findings, and conclusions or recommendations expressed in this material are those of the author(s) and do not necessarily reflect the views of the National Science Foundation.

■ REFERENCES

(1) Sung, H.; Ferlay, J.; Siegel, R. L.; et al. Global Cancer Statistics 2020: GLOBOCAN Estimates of Incidence and Mortality Worldwide for 36 Cancers in 185 Countries. *CA-Cancer J. Clin.* **2021**, *71*, 209–249.

(2) Trayes, K. P.; Cokenakes, S. E. Breast Cancer Treatment. *Am. Fam. Physician* **2021**, *104*, 171–178.

(3) Jerusalem, G.; Lancellotti, P.; Kim, S. B. HER2+ breast cancer treatment and cardiotoxicity: monitoring and management. *Breast Cancer Res. Treat.* **2019**, *177*, 237–250.

(4) Huang, H.; Lovell, J. F. Advanced Functional Nanomaterials for Theranostics. *Adv. Funct. Mater.* **2017**, *27*, No. 1603524.

(5) Phillips, W. T.; Bao, A.; Brenner, A. J.; Goins, B. A. Image-guided interventional therapy for cancer with radiotherapeutic nanoparticles. *Adv. Drug Delivery Rev.* **2014**, *76*, 39–59.

(6) Funkhouser, J. Reinventing pharma: The theranostic revolution. *Curr. Drug Discovery* **2002**, *2*, 17–19.

(7) Huang, J.; Li, Y.; Orza, A.; Lu, Q.; Guo, P.; Wang, L.; Yang, L.; Mao, H. Magnetic Nanoparticle Facilitated Drug Delivery for Cancer Therapy with Targeted and Image-Guided Approaches. *Adv. Funct. Mater.* **2016**, *26*, 3818–3836.

(8) Aghaee, F.; Islamian, J. P.; Baradaran, B.; Mesbahi, A.; Mohammadzadeh, M.; Jafarabadi, M. A. Enhancing the Effects of Low Dose Doxorubicin Treatment by the Radiation in T47D and SKBR3 Breast Cancer Cells. *J. Breast Cancer* **2013**, *16*, 164–170.

(9) Ahmad, I.; Mustafa, E.; Mustafa, N.; Tahtamouni, L.; Abdalla, M. 2DG enhances the susceptibility of breast cancer cells to doxorubicin. *Cent. Eur. J. Biol.* **2010**, *5*, 739–748.

(10) Miller, J. P.; Maji, D.; Lam, J.; Tromberg, B. J.; Achilefu, S. Noninvasive depth estimation using tissue optical properties and a dual-wavelength fluorescent molecular probe in vivo. *Biomed. Opt. Express* **2017**, *8*, 3095–3109.

(11) Ntziachristos, V. Going deeper than microscopy: the optical imaging frontier in biology. *Nat. Methods* **2010**, *7*, 603–614.

(12) Terreno, E.; Castelli, D. D.; Viale, A.; Aime, S. Challenges for Molecular Magnetic Resonance Imaging. *Chem. Rev.* **2010**, *110*, 3019–3042.

(13) Lawrence, T. S.; Buckner, J. C.; Lang, F. F. CNS malignancies: At last, real progress. *J. Clin. Oncol.* **2006**, *24*, 1225–1227.

(14) Shamsi, M.; Pirayesh, I. J. Breast cancer: Early diagnosis and effective treatment by drug delivery tracing. *Nucl. Med. Rev.* **2017**, *20*, 45–48.

(15) Phua, V. J. X.; Yang, C.-T.; Xia, B.; Yan, S. X.; Liu, J.; Aw, S. E.; He, T.; Ng, D. C. E. Nanomaterial Probes for Nuclear Imaging. *Nanomaterials* **2022**, *12*, No. 582.

(16) Wang, H. T.; Kumar, R.; Nagesha, D.; Duclos, R. I.; Sridhar, S.; Gatley, S. J. Integrity of 111ln-radiolabeled superparamagnetic iron oxide nanoparticles in the mouse. *Nucl. Med. Biol.* **2015**, *42*, 65–70.

(17) Pellico, J.; Ruiz-Cabello, J.; Saiz-Alía, M.; Del Rosario, G.; Caja, S.; Montoya, M.; Fernández de Manuel, L.; Morales, M. P.; Gutiérrez, L.; Galiana, B.; Enríquez, J. A.; Herranz, F. Fast synthesis and bioconjugation of 68Ga core-doped extremely small iron oxide nanoparticles for PET/MR imaging. *Contrast Media Mol. Imaging* **2016**, *11*, 203–210.

(18) Burke, B. P.; Cawthorne, C.; Archibald, S. J. Multimodal nanoparticle imaging agents: Design and applications. *Philos. Trans. R. Soc., A* **2017**, *375*, No. 20170261.

(19) Choi, H.; Lee, Y. S.; Hwang, D. W.; Lee, D. S. Translational radionanomedicine: A clinical perspective. *Eur. J. Nanomed.* **2016**, *8*, 71–84.

(20) Andersen, T. L.; Baun, C.; Olsen, B. B.; Dam, J. H.; Thisgaard, H. Improving contrast and detectability: Imaging with [55Co] Co-DOTATATE in comparison with [64Cu] Cu-DOTATATE and [68Ga] Ga-DOTATATE. *J. Nucl. Med.* **2020**, *61*, 228–233.

(21) Jødal, L.; Le Loirec, C.; Champion, C. Positron Range in PET Imaging: Non-Conventional Isotopes. *Phys. Med. Biol.* **2014**, *59*, 7419–7434.

(22) Ali, I.; Alsehli, M.; Scotti, L.; Tullius Scotti, M.; Tsai, S.-T.; Yu, R.-S.; Hsieh, M. F.; Chen, J.-C. Progress in Polymeric Nano-Medicines for Theranostic Cancer Treatment. *Polymers* **2020**, *12*, No. 598.

(23) Anchordoquy, T. J.; Barenholz, Y.; Boraschi, D.; Chorny, M.; Decuzzi, P.; Dobrovolskaia, M. A.; Farhangrazi, Z. S.; Farrell, D.; Gabizon, A.; Ghandehari, H.; Godin, B.; La-Beck, N. M.; Ljubimova, J.; Moghimi, S. M.; Pagliaro, L.; Park, J. H.; Peer, D.; Ruoslahti, E.; Serkova, N. J.; Simberg, D. Mechanisms and Barriers in Cancer Nanomedicine: Addressing Challenges, Looking for Solutions. *ACS Nano* **2017**, *11*, 12–18.

(24) Che, H.; van Hest, J. C. Stimuli-responsive polymersomes and nanoreactors. *J. Mater. Chem. B* **2016**, *4*, 4632–4647.

(25) Youssef, S. F.; Elnaggar, Y. S.; Abdallah, O. Y. Elaboration of polymersomes versus conventional liposomes for improving oral bioavailability of the anticancer flutamide. *Nanomedicine* **2018**, *13*, 3025–3036.

(26) Himanshu, A.; Sitasharan, P.; Singhai, A. Liposomes as drug carriers. *IJPLS* **2011**, *2*, 945–951.

(27) Hu, X.; Zhang, Y.; Xie, Z.; Jing, X.; Bellotti, A.; Gu, Z. Stimuli-Responsive Polymersomes for Biomedical Applications. *Biomacromolecules* **2017**, *18*, 649–673.

(28) Wang, X.; Hu, J.; Liu, S. Overcoming the Dilemma of Permeability and Stability of Polymersomes through Traceless Cross-Linking. *Acc. Chem. Res.* **2022**, *55*, 3404–3416.

(29) Perera, R. M.; Gupta, S.; Li, T.; Bleuel, M.; Hong, K.; Schneider, G. J. Influence of NaCl on shape deformation of polymersomes. Soft Matter. *Soft Matter* **2021**, *17*, 4452–4463.

(30) Gebhardt, K. E.; Ahn, S.; Venkatachalam, G.; Savin, D. A. Role of Secondary Structure Changes on the Morphology of Polypeptide-

Based Block Copolymer Vesicles. *J. Colloid Interface Sci.* **2008**, *317*, 70−76.

(31) Chidanguro, T.; Simon, Y. C. Bent out of shape: Towards non-spherical polymersome morphologies. *Polym. Int.* **2021**, *70*, 951−957.

(32) Pearson, R. T.; Warren, N. J.; Lewis, A. L.; Armes, S. P.; Battaglia, G. Effect of pH and Temperature on PMPC-PDPA Copolymer Self-Assembly. *Macromolecules* **2013**, *46*, 1400−1407.

(33) Liu, F.; Kozlovskaya, V.; Medipelli, S.; Xue, B.; Ahmad, F.; Saeed, M.; Cropek, D.; Kharlampieva, E. Temperature-sensitive polymersomes for controlled delivery of anticancer drugs. *Chem. Mater.* **2015**, *27*, 7945−7956.

(34) Yang, Y.; Alford, A.; Kozlovskaya, V.; Zhao, S.; Joshi, H.; Kim, E.; Qian, S.; Urban, V.; Cropek, D.; Aksimentiev, A.; Kharlampieva, E. Effect of Temperature ad Hydrophilic Ratio on the Structure of Poly(N-vinylcaprolactam)-block-poly(dimethylsiloxane)-block-poly(N-vinylcaprolactam) Polymersomes. *ACS Appl. Polym. Mater.* **2019**, *1*, 722−736.

(35) Yang, Y.; Kozlovskaya, V.; Dolmat, M.; Song, Y.; Qian, S.; Urban, V.; Cropek, D.; Kharlampieva, E. Temperature Controlled Transformations of Giant Unilamellar Vesicles of Amphiphilic Triblock Copolymers Synthesized via Microfluididc Mixing. *Appl. Surf. Sci. Adv.* **2021**, *5*, No. 100101.

(36) Kozlovskaya, V.; Liu, F.; Yang, Y.; Ingle, K.; Qian, S.; Halade, G. V.; Urban, V. S.; Kharlampieva, E. Temperature-responsive polymersomes of poly (3-methyl-N-vinylcaprolactam)-block-poly (N-vinylpyrrolidone) to decrease doxorubicin-induced cardiotoxicity. *Biomacromolecules* **2019**, *20*, 3989−4000.

(37) Byrne, J. D.; Betancourt, T.; Brannon-Peppas, L. Active targeting schemes for nanoparticle systems in cancer therapeutics. *Adv. Drug Delivery Rev.* **2008**, *60*, 1615−1626.

(38) Xue, B.; Kozlovskaya, V.; Sherwani, M. A.; Ratnayaka, S.; Habib, S.; Anderson, T.; Manuvakhova, M.; Klampfer, L.; Yusuf, N.; Kharlampieva, E. Peptide-functionalized hydrogel cubes for active tumor cell targeting. *Biomacromolecules* **2018**, *19*, 4084−4097.

(39) Burguin, A.; Furrer, D.; Ouellette, G.; Jacob, S.; Diorio, C.; Durocher, F. Trastuzumab effects depend on HER2 phosphorylation in HER2-negative breast cancer cell lines. *PLoS One* **2020**, *15*, No. e0234991.

(40) Cho, H.-S.; Mason, K.; Ramyar, K. X.; Stanley, A. M.; Gabelli, S. B.; Denney, D. W., Jr; Leahy, D. J. Structure of the extracellular region of HER2 alone and in complex with the Herceptin Fab. *Nature* **2003**, *421*, 756−760.

(41) Psimadas, D.; Oliveira, H.; Thevenot, J.; Lecommandoux, S.; Bouziotis, P.; Varvarigou, A. D.; Georgoulias, P.; Loudos, G. Polymeric micelles and vesicles: Biological behavior evaluation using radiolabeling techniques. *Pharm. Dev. Technol.* **2014**, *19*, 189−193.

(42) Peltek, O. O.; Muslimov, A. R.; Zyuzin, M. V.; Timin, A. S. Current Outlook on Radionuclide Delivery Systems: From Design Consideration to Translation into Clinics. *J. Nanobiotechnol.* **2019**, *17*, No. 90.

(43) Starmans, L. W. E.; Hummelink, M. A.; Rossin, R.; Kneepkens, E. C.; Lamerichs, R.; Donato, K.; Nicolay, K.; Grüll, H. 89 Zr- and Fe-Labeled Polymeric Micelles for Dual Modality PET and T 1 -Weighted MR Imaging. *Adv. Healthcare Mater.* **2015**, *4*, 2137−2145.

(44) Roobol, S. J.; Hartjes, T. A.; Slotman, J. A.; de Kruijff, R. M.; Torrelo, G.; Abraham, T. E.; Bruchertseifer, F.; Morgenstern, A.; Kanaar, R.; van Gent, D. C.; Houtsmuller, A. B.; Denkova, A. G.; van Royen, M. E.; Essers, J. Uptake and subcellular distribution of radiolabeled polymersomes for radiotherapy. *Nanotheranostics* **2020**, *4*, 14−25.

(45) Wong, R. M.; Gilbert, D. A.; Liu, K.; Louie, A. Y. Rapid Size-Controlled Synthesis of Dextran-Coated, 64Cu-Doped Iron Oxide Nanoparticles. *ACS Nano* **2012**, *6*, 3461−3467.

(46) Cheng, L.; Shen, S.; Jiang, D.; Jin, Q.; Ellison, P. A.; Ehlerding, E. B.; Goel, S.; Song, G.; Huang, P.; Barnhart, T. E.; Liu, Z.; Cai, W. Chelator-Free Labeling of Metal Oxide Nanostructures with Zirconium-89 for Positron Emission Tomography Imaging. *ACS Nano* **2017**, *11*, 12193−12201.

(47) Chen, F.; Ellison, P. A.; Lewis, C. M.; Hong, H.; Zhang, Y.; Shi, S.; Hernandez, R.; Meyerand, M. E.; Barnhart, T. E.; Cai, W. Chelator-free synthesis of a dual-modality PET/MRI agent. *Angew. Chem., Int. Ed.* **2013**, *52*, 13319−13323.

(48) Shaffer, T. M.; Wall, M. A.; Harmsen, S.; Longo, V. A.; Drain, C. M.; Kircher, M. F.; Grimm, J. Silica nanoparticles as substrates for chelator-free labeling of oxophilic radioisotopes. *Nano Lett.* **2015**, *15*, 864−868.

(49) Tang, T.; Wei, Y.; Yang, Q.; Yang, Y.; Sailor, M. J.; Pang, H.-B. Rapid chelator-free radiolabeling of quantum dots for in vivo imaging. *Nanoscale* **2019**, *11*, 22248−22254.

(50) Abou, D. S.; Thorek, D. L.; Ramos, N. N.; Pinkse, M. W.; Wolterbeek, H. T.; Carlin, S. D.; Beattie, B. J.; Lewis, J. S. 89Zr-Labeled Paramagnetic Octreotide-Liposomes for PET-MR Imaging of Cancer. *Pharm. Res.* **2013**, *30*, 878−888.

(51) Khan, A. A.; Man, F.; Faruqu, F. N.; Kim, J.; Al-Salemee, F.; Carrascal-Miniño, A.; Volpe, A.; Liam-Or, R.; Simpson, P.; Fruhwirth, G. O.; Al-Jamal, K. T.; de Rosales, R. T. M. PET Imaging of Small Extracellular Vesicles via [89Zr]Zr(oxinate)$_4$ Direct Radiolabeling. *Bioconjugate Chem.* **2022**, *33*, 473−485.

(52) Yang, Y.; Kozlovskaya, V.; Zhang, Z.; Xing, C.; Zaharias, S.; Dolmat, M.; Qian, S.; Zhang, J.; Warram, J. M.; Yang, E. S.; Kharlampieva, E. Poly(N-vinylpyrrolidone)-block-poly(dimethylsiloxane)-block-poly(N-vinylpyrrolidone) Triblock Copolymer Polymersomes for Delivery of PARP1 siRNA to Breast Cancers. *ACS Appl. Bio Mater.* **2022**, *5*, 1670−1682.

(53) Liu, F.; Kozlovskaya, V.; Zavgorodnya, O.; Martinez-Lopez, C.; Catledge, S.; Kharlampieva, E. Encapsulation of anticancer drug with hydrogen-bonded multilayers of tannic acid. *Soft Matter* **2014**, *10*, 9237−9247.

(54) Kozlovskaya, V.; Xue, B.; Lei, W.; Padgett, L. E.; Tse, H. M.; Kharlampieva, E. Hydrogen-Bonded Multilayers of Tannic Acid as Mediators of T Cell Immunity. *Adv. Healthcare Mater.* **2015**, *4*, 686−694.

(55) Feduska, J. M.; Kozlovskaya, V.; Alford, A.; Padgett, L. E.; Kharlampieva, E.; Tse, H. M. Dampening antigen-specific T cell responses with antigens encapsulated in polyphenolic capsules. *ImmunoHorizons* **2020**, *4*, 530−545.

(56) Alford, A.; Kozlovskaya, V.; Xue, B.; Gupta, N.; Higgins, W.; Pham-Hua, D.; He, L.; Urban, V. S.; Tse, H. M.; Kharlampieva, E. Manganoporphyrin-Polyphenol Multilayer Capsules as Radical and Reactive Oxygen Species (ROS) Scavengers. *Chem. Mater.* **2018**, *30*, 344−357.

(57) Barra, J. M.; Kozlovskaya, V.; Kharlampieva, E.; Tse, H. M. Localized Immunosuppression with Tannic Acid Encapsulation Delays Islet Allograft and Autoimmune-mediated Rejection. *Diabetes* **2020**, *69*, 1948−1960.

(58) Liang, X.; Kozlovskaya, V.; Cox, C. P.; Wang, Y.; Saeed, M.; Kharlampieva, E. Synthesis and Self-Assembly of Thermosensitive Double-hydrophilic Poly(N-vinylcaprolactam)-b-poly(N-vinyl-2-pyrrolidone) Diblock Copolymers. *J. Polym. Sci., Part A: Polym. Chem.* **2014**, *52*, 2725−2737.

(59) Kozlovskaya, V.; Yang, Y.; Liu, F.; Ingle, K.; Ahmad, A.; Halade, G. V.; Kharlampieva, E. Dually Responsive Poly(N-vinylcaprolactam)-b-poly(dimethylsiloxane)-b-poly(N-vinylcaprolactam) Polymersomes for Controlled Delivery. *Molecules* **2022**, *27*, No. 3485.

(60) Lai, Y. C.; Ozark, R.; Quinn, E. T. Synthesis and characterization of α, ω-bis (4-ydroxybutyl) polydimethylsiloxanes. *J. Polym. Sci., Part A: Polym. Chem.* **1995**, *33*, 1773−1782.

(61) Queern, S. L.; Aweda, T. A.; Massicano, A. V. F.; Clanton, N. A.; El Sayed, R.; Sader, J. A.; Zyuzin, A.; Lapi, S. E. Production of Zr-89 Using Sputtered Yttrium Coin Targets. *Nucl. Med. Biol.* **2017**, *50*, 11−16.

(62) Wooten, A. L.; Lewis, B. C.; Szatkowski, D. J.; Sultan, D. H.; Abdin, K. I.; Voller, T. F.; Liu, Y.; Lapi, S. E. Calibration Setting Numbers for Dose Calibrators for the PET Isotopes 52Mn, 64Cu, 76Br, 86Y, 89Zr, 124I. *Appl. Radiat. Isot.* **2016**, *113*, 89−95.

(63) Allen, S.; Osorio, O.; Liu, Y. G.; Scott, E. Facile assembly and loading of theranostic polymersomes via multi-impingement flash nanoprecipitation. *J. Controlled Release* **2017**, *262*, 91−103.

(64) Kozlovskaya, V.; Liu, F.; Xue, B.; Ahmad, F.; Alford, A.; Saeed, M.; Kharlampieva, E. Polyphenolic polymersomes of temperature-sensitive poly(N-vinylcaprolactam)-block-(poly(N-vinylpyrrolidone) for anticancer therapy. *Biomacromolecules* **2017**, *18*, 2552−2563.

(65) Osawa, R.; Walsh, T. P. Effects of Acidic and Alkaline Treatments on Tannic Acid and Its Binding Property to Protein. *J. Agric. Food Chem.* **1993**, *41*, 704−707.

(66) Shukla, A.; Fang, J. C.; Puranam, S.; Jensen, F. R.; Hammond, P. T. Hemostatic Multilayer Coatings. *Adv. Mater.* **2012**, *24*, 492−496.

(67) Hofmann, T.; Glabasnia, A.; Schwarz, B.; Wisman, K. N.; Gangwer, K. A.; Hagerman, A. E. Protein binding and astringent taste of a polymeric procyanidin, 1, 2, 3, 4, 6-penta-O-galloyl-β-D-glucopyranose, castalagin, and grandinin. *J. Agric. Food Chem.* **2006**, *54*, 9503−9509.

(68) Barra, J. M.; Kozlovskaya, V.; Burnette, K. S.; Banerjee, R.; Fraker, C. A.; Kharlampieva, E.; Tse, H. M. Localized cytotoxic T cell−associated antigen 4 and antioxidant islet encapsulation alters macrophage signaling and induces regulatory and anergic T cells to enhance allograft survival *Am. J. Transplant.* **2023**, DOI: 10.1016/j.ajt.2023.01.007.

(69) Erel-Unal, I.; Sukhishvili, S. A. Hydrogen-Bonded Multilayers of a Neutral Polymer and a Polyphenol. *Macromolecules* **2008**, *41*, 3962−3970.

(70) Shutava, T.; Prouty, M.; Kommireddy, D.; Lvov, Y. pH Responsive Decomposable Layer-by-Layer Nanofilms and Capsules on the Basis of Tannic Acid. *Macromolecules* **2005**, *38*, 2850−2858.

(71) Liu, Z.; Song, Y.; Li, D. Detecting zeta potential of polydimethylsiloxane (PDMS) in electrolyte solutions with atomic force microscope. *J. Colloid Interface Sci.* **2020**, *578*, 116−123.

(72) Kozlovskaya, V.; Yakovlev, S.; Libera, M.; Sukhishvili, S. A. Surface Priming and the Self-Assembly of Hydrogen-Bonded Multilayer Capsules and Films. *Macromolecules* **2005**, *38*, 4828−4836.

(73) Lin, D.; Liu, N.; Yang, K.; Zhu, L.; Xu, Y.; Xing, B. The effect of ionic strength and pH on the stability of tannic acid-facilitated carbon nanotube suspensions. *Carbon* **2009**, *47*, 2875−2882.

(74) Ramos, J.; Vega, J. F.; Cruz, V.; Sanchez-Sanchez, E.; Cortes, J.; Martinez-Salazar, J. Hydrodynamic and Electrophoretic Properties of Trastuzumab/HER2 Extracellular Domain Complexes as Revealed by Experimental Techniques and Computational Simulations. *Int. J. Mol. Sci.* **2019**, *20*, No. 1076.

(75) Maeda, H.; Nakamura, H.; Fang, J. The EPR effect for macromolecular drug delivery to solid tumors: Improvement of tumor uptake, lowering of systemic toxicity, and distinct tumor imaging in vivo. *Adv. Drug Delivery Rev.* **2013**, *65*, 71−79.

(76) Guo, J.; Ping, Y.; Ejima, H.; Alt, K.; Meissner, M.; Richardson, J. J.; Yan, Y.; Peter, K.; Von Elverfeldt, D.; Hagemeyer, C. E.; Caruso, F. Engineering multifunctional capsules through the assembly of metal-phenolic networks. *Angew. Chem., Int. Ed.* **2014**, *53*, 5546−5551.

(77) Kozlovskaya, V.; Alford, A.; Dolmat, M.; Ducharme, M.; Caviedes, R.; Radford, L.; Lapi, S.; Kharlampieva, E. Multilayer microcapsules with shell-chelated 89Zr for PET imaging and controlled delivery. *ACS Appl. Mater. Interfaces* **2020**, *12*, 56792−56804.

(78) Guo, L.; Yan, B.; Liu, J.-L.; Sheng, K.; Wang, X.-L. Coordination bonding construction, characterization and photo-luminescence of ternary lanthanide (Eu3+, Tb 3+) hybrids with phenylphenacyl-sulfoxide modified bridge and polymer unit. *Dalton Trans.* **2011**, *40*, 632−638.

(79) Geng, H.; Zhong, Q.-Z.; Li, J.; Lin, Z.; Cui, J.; Caruso, F.; Hao, J. Metal Ion-Directed Functional Metal-Phenolic Materials. *Chem. Rev.* **2022**, *122*, 11432−11473.

(80) Holten-Andersen, N.; Harrington, M. J.; Birkedal, H.; Lee, B. P.; Messersmith, P. B.; Lee, K. Y. C.; Waite, J. H. pH-Induced Metal-Ligand Cross-Links Inspired by Mussel Yield Self-Healing Polymer Networks with Near-Covalent Elastic Moduli. *Proc. Natl. Acad. Sci. U.S.A.* **2011**, *108*, 2651−2655.

(81) Cvjetinović, Đ.; Prijović, Ž.; Janković, D.; Radović, M.; Mirković, M.; Milanović, Z.; Mojović, M.; Škalamera, Đ.; Vranješ-Đurić, S. Bioevaluation of glucose-modified liposomes as a potential drug delivery system for cancer treatment using 177-Lu radiotracking. *J. Controlled Release* **2021**, *332*, 301−311.

(82) Larenkov, A.; Bubenschikov, V.; Makichyan, A.; Zhukova, M.; Krasnoperova, A.; Kodina, G. Preparation of Zirconium-89 Solutions for Radiopharmaceutical Purposes: Interrelation Between Formulation, Radiochemical Purity, Stability and Biodistribution. *Molecules* **2019**, *24*, 1534−1558.

(83) Abou, D. S.; Ku, T.; Smith-Jones, P. In Vivo Biodistribution and Accumulation of 89Zr in Mice. *Nucl. Med. Biol.* **2011**, *38*, 675−681.

(84) Severin, G. W.; Jørgensen, J. T.; Wiehr, S.; Rolle, A.-M.; Hansen, A. E.; Maurer, A.; Hasenberg, M.; Pichler, B.; Kjaer, A.; Jensen, A. I. The impact of weakly bound 89Zr on preclinical studies: Non-specific accumulation in solid tumors and aspergillus infection. *Nucl. Med. Biol.* **2015**, *42*, 360−368.

(85) Price, E. W.; Orvig, C. Matching Chelators to Radiometals for Radiopharmaceuticals. *Chem. Soc. Rev.* **2014**, *43*, 260−290.

(86) Du, B.; Jiang, X.; Das, A.; Zhou, Q.; Yu, M.; Jin, R.; Zheng, J. Glomerular barrier behaves as an atomically precise bandpass filter in a sub-nanometre regime. *Nat. Nanotechnol.* **2017**, *12*, 1096−1102.

(87) Hinton, T. M.; Monaghan, P.; Green, D.; Kooijmans, S. A. A.; Shi, S.; Breheney, K.; Tizard, M.; Nicolazzo, J. A.; Zelikin, A. N.; Wark, K. Biodistribution of Polymer Hydrogel Capsules for the Delivery of Therapeutics. *Acta Biomater.* **2012**, *8*, 3251−3260.

(88) Sindeeva, O. A.; Verkhovskii, R. A.; Abdurashitov, A. S.; Voronin, D. V.; Gusliakova, O. I.; Kozlova, A. A.; Mayorova, O. A.; Ermakov, A. V.; Lengert, E. V.; Navolokin, N. A.; Tuchin, V. V.; Gorin, D. A.; Sukhorukov, G. B.; Bratashov, D. N. Effect of Systemic Polyelectrolyte Microcapsule Administration on the Blood Flow Dynamics of Vital Organs. *ACS Biomater. Sci. Eng.* **2020**, *6*, 389−397.

(89) Pérez-Medina, C.; Tang, J.; Abdel-Atti, D.; Hogstad, B.; Merad, M.; Fisher, E. A.; Fayad, Z. A.; Lewis, J. S.; Mulder, W. J.; Reiner, T. PET Imaging of Tumor-Associated Macrophages with 89Zr-Labeled High-Density Lipoprotein Nanoparticles. *J. Nucl. Med.* **2015**, *56*, 1272−1277.

(90) Austin, C. D.; De Mazière, A. M.; Pisacane, P. I.; van Dijk, S. M.; Eigenbrot, C.; Sliwkowski, M. X.; Klumperman, J.; Scheller, R. H. Endocytosis and sorting of ErbB2 and the site of action of cancer therapeutics trastuzumab and geldanamycin. *Mol. Biol. Cell* **2004**, *15*, 5268−5282.

(91) Burguin, A.; Furrer, D.; Ouellette, G.; Jacob, S.; Diorio, C.; Durocher, F. Trastuzumab effects depend on HER2 phosphorylation in HER2-negative breast cancer cell lines. *PLoS One* **2020**, *15*, No. e0234991.